Multidisciplinary Applications Using Multibody Dynamics as the Framework for Developments

Jorge Ambrósio

IDMEC - Instituto Superior Técnico, Av. Rovisco Pais, 1049-001 Lisboa, Portugal

Abstract: The structure of the equations of motion of multibody systems allows the incorporation of the equilibrium equations of a large number of disciplines and their solution in a combined form. The description of the structural deformations exhibited by the system components by using linear or non-linear finite elements in the framework of multibody dynamics is an example of the integration of the equations of equilibrium of different specialties. Of particular importance in the applications pursued with the methodologies proposed is the treatment of contact and impact which are introduced in the multibody systems equations either by using unilateral constraints or by applying a continuous contact force model. The readily availability of the state variables in the multibody formulation allows for the use of different control paradigms in the framework of vehicle dynamics, biomechanics or robotics and their easy integration with the multibody equations. Application cases involving the modeling of realistic systems, passive safety of road and rail vehicles, automotive and railway dynamics and flexible multibody systems demonstrate the developments listed in this presentation. In the process of presenting the different applications potential future developments are discussed.

Keywords: flexible multibody dynamics, vehicle dynamics, contact, passive safety.

NOMENCLATURE

A matrices are boldface upper-case
a vectors are boldface lower-case
a, α scalars are lightface characters

Symbols

$\mathbf{A}_i$ Transformation matrix from body I

I 3x3 identity matrix

$\mathbf{M}_i$ 6x6 mass matrix of body i

M Mass matrix of a system

$\mathbf{f}_i$ Force acting in body i, in global coordinates

$\mathbf{g}_i$ Vector of forces for body i containing $\mathbf{f}_i$ and $\mathbf{n}_i$

g Vector of forces for a system

$\mathbf{n}_i$ Moment acting in body i, in global coordinates

$\mathbf{n}'_i$ Moment acting in body i, in body coordinates

$\mathbf{p}_i$ Vector with the four Euler parameters of body i

$\mathbf{q}_i$ Vector of coordinates for body i

$\mathbf{q}$ Vector of coordinates of a system

$\mathbf{q}_r$ Vector of rigid body coordinates for a system

$\mathbf{q}_f$ Vector of flexible body coordinates for a system

$\mathbf{r}_i$ Vector of translation coordinates for body i

γ Vector of right-hand side of the acceleration constraint equations

ν Vector of right-hand side of the velocity constraint equations

λ Vector of Lagrange multipliers

ω_i Vector with the angular velocity of body i

Φ Vector of kinematic constraints

D Jacobian matrix of constraints

Overscores

$\rightarrow$ Geometric vector

~ 3x3 skew symmetric matrix

. First time derivative.

.. Second time derivative

Superscripts

−1 Matrix inverse.

i i^{th} time step

T Matrix transpose

′ Components of the vector are in a body-fixed coordinate system

Subscripts

i i^{th} body in the system

f Flexible body quantity

r Rigid body quantity

INTRODUCTION

In multibody dynamics methods body fixed coordinate frames are generally adopted to position each one of the system components and to allow for the specification of the kinematic constraints that represent the restrictions on the relative motion between the bodies (Nikravesh, 1988). Several formalisms suggest the use of different sets of coordinates, such as Cartesian, natural and relative coordinates (Jalón and Bayo, 1994; Nikravesh and Gim, 1993; Nikravesh and Ambrósio, 1992; Kane and Levinson, 1985). Depending on the type of applications pursued by the user, on the experience of the developer or on any specific objectives each one of the referred types of coordinates has advantages and disadvantages relative to the others. Due to their ease of computational implementation, their physical meaning and the wide spread knowledge of their features all the formalisms presented in this work are based on the use of Cartesian coordinates (Nikravesh, 1988). The equations of motion of the multibody systems can be obtained using the Euler-Lagrange equations or the principle of virtual works. Kinematic constraints that restrict the relative motion between the different components of the system are added to the equilibrium equations by using Lagrange multipliers. The set of equations obtained in this manner, together with the acceleration constraint equations, are solved to obtain the system accelerations. The system state variables are then integrated in time, typically using a variable order and variable time step integration algorithm for a pre-defined period of time.

The multibody dynamics procedures formulated in the form briefly described before have not only all the ingredients to allow modeling typical mechanisms but also to incorporate methods generally associated to other disciplines. The contact between different bodies of the system or with other objects can be described in the framework of multibody dynamics as a set of external forces applied to the bodies in contact, using some form of penalty formulation (Lankarani and Nikravesh, 1994), or as a unilateral constraint, therefore involving the definition of kinematic constraints (Pfeiffer and Glocker, 1996). The internal forces that develop in the human body due to muscle, ligaments, tendons are also described in the framework of multibody dynamics through biomechanical models where most of the anatomical joints are modeled as mechanical joints or contact pairs, ligaments are described as force elements while the muscles and their actions are represented either as force elements or as time dependent kinematic constraints (Ambrósio and Silva, 2005). Also, the control theory finds in the multibody dynamics formulations efficient descriptions not only for the mathematical surrogates of the systems that are the object of the control but also for the controllers. Such as before, the control actions over the system may be through inputs involving the state variables or by applying forces on the system components (Antos and Ambrósio, 2004; Huyge et al., 2005; Brüls et al., 2006)).

The flexible multibody dynamics represents another area where traditional multibody formalisms serve as the base to integrate approaches typically associated to structural mechanics, such as the finite element method. Methodologies to describe the flexibility of multibody systems using the finite segment approach (Huston and Wang, 1994) in case of linear deformations or the plastic hinge approach (Nikravesh et al., 1983; Ambrósio et al., 1996a) in the case of nonlinear deformations exemplify some of the earlier methodologies, still with a good ground for application today. Better known are the finite element approaches to flexible multibody dynamics that deal with the linear elastodynamics of the system using different forms of substructuring and reduction techniques (Song and Haug, 1980; Yoo and Haug, 1986; Shabana, 1989; Gonçalves and Ambrósio, 2001; Géradin and Cardona, 2001), or with nonlinear deformations, including material and geometric nonlinearities (Ambrósio, 1996b, 2000; Cardona and Géradin, 1988; Mikkola and Shabana, 2003).

The applications of the multibody formalisms presented in this work include vehicle dynamics, biomechanics, deformable space structures and structural crashworthiness and represent the research carried at IDMEC in different collaborative works. Starting from the description of the rigid multibody system different problems in the area of rail guided vehicle dynamics are formulated and solved. For each one of the problems solved a new feature of the multibody formulation is described and applied in order to demonstrate the ability that a general multibody system has to describe a wide range of situations. In the process kinematic constraints representing situations as diverse as vehicle prescribed trajectories or muscle actuator elements are presented. The contact problem present in many important applications of multibody dynamics is also described here in the framework of vehicle impact, rail-wheel contact and catenary-pantograph contact. Finally, in the frameworks of vehicle structural crashworthiness and of flexible space structures a formulation for flexible multibody systems based on a finite element approach is presented and demonstrated.

RIGID MULTIBODY DYNAMICS FORMULATION

A multibody system is defined as a collection of rigid and/or flexible bodies constrained by kinematic joints and eventually acted upon by internal and/or external forces, as depicted in Fig. 1. The position and orientation of a body *i* in space are described by a position vector $\mathbf{r}_i$ and a set of rotational coordinates $\mathbf{p}_i$, which are organized in a vector as (Nikravesh, 1988):

$$\mathbf{q}_i = [\mathbf{r}^T , \mathbf{p}^T]_i^T \tag{1}$$

According with this definition, a multibody system with *nb* bodies is described by a set of coordinates in the form:

$$\mathbf{q} = [\mathbf{q}_1^T, \mathbf{q}_2^T, \cdots, \mathbf{q}_{nb}^T]^T \tag{2}$$

The dependencies among system coordinates, which result from the existence of mechanical joints interconnecting the several bodies, are defined through the introduction of kinematic relationships written as:

$$\mathbf{\Phi}(\mathbf{q}, t) = \mathbf{0} \tag{3}$$

where *t* is the time variable, which is used only for the driving constraints. The second time derivative of Eq. (3) with respect to time yields:

$$\ddot{\mathbf{\Phi}}(\mathbf{q}, \dot{\mathbf{q}}, \ddot{\mathbf{q}}, t) = \mathbf{0} \equiv \mathbf{D}\,\ddot{\mathbf{q}} = \mathbf{\gamma} \tag{4}$$

where **D** is the Jacobian matrix of the constraints, $\ddot{\mathbf{q}}$ is the acceleration vector and $\mathbf{\gamma}$ is the vector that depends on the velocities and time.
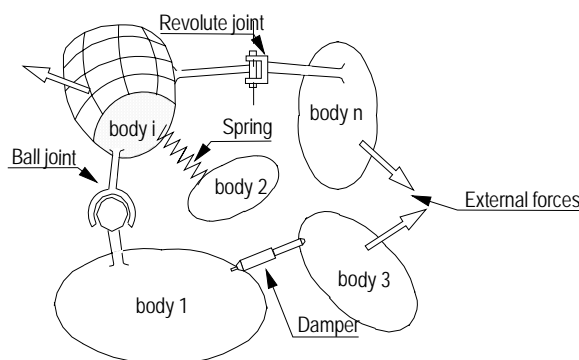
Figure 1 - Generic multibody system

The system kinematic constraints are added to the equations of motion using the Lagrange multipliers technique. Defining by λ the vector of the unknown Lagrange multipliers, the equations of motion for a mechanical system are

$$\begin{bmatrix} \mathbf{M} & \mathbf{D}^T \\ \mathbf{D} & \mathbf{0} \end{bmatrix} \begin{Bmatrix} \ddot{\mathbf{q}} \\ \lambda \end{Bmatrix} = \begin{Bmatrix} \mathbf{f} \\ \gamma \end{Bmatrix} \tag{5}$$

where $\mathbf{M}$ is the global mass matrix, containing the mass and moments of inertia of all bodies, and $\mathbf{f}$ is the force vector, containing all forces and moments applied on system bodies plus the gyroscopic forces. The Lagrange multipliers, associated to the kinematic constraints, are physically related with the reaction forces generated between the bodies interconnected by kinematic joints, given by

$$\mathbf{f}^{(c)} = -\mathbf{D}^T \lambda \tag{6}$$

The usual procedures to handle the integration of sets of differential-algebraic equations must still be applied in this case in order to eliminate the constraint drift or to maintain it under control (Nikravesh, 1988; Jalon and Bayo, 1994).

Solution of the equations of motion

The forward dynamic analysis of a multibody system requires that the initial conditions of the system, i.e. the position vector $\mathbf{q}^0$ and the velocity vector $\dot{\mathbf{q}}^0$, are given. With this information Eq. (5) is assembled and solved for the unknown accelerations, which are in turn integrated in time together with the velocities. The process, schematically shown in Fig. 2, proceeds until the system response is obtained for the analysis period.
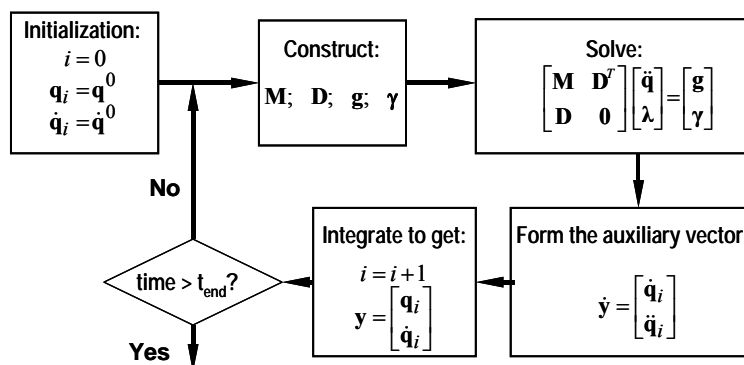

Figure 2 - Flowchart representing the forward dynamic analysis of a multibody system.

NORMAL CONTACT PROBLEM

A large number of interesting applications of multibody dynamics require an appropriate description of the contact phenomena. Most of such applications require a model for the normal contact forces before any description of the tangential forces is possible. Such is the case of rail-wheel contact mechanics, tire contact mechanics or tribological contact models in machine design. A model for the contact force must consider the material and geometric properties of the surfaces, contribute to a stable integration and account for some level of energy dissipation. Based on an Hertzian description of the contact forces between two solids Lankarani and Nikravesh (1994) propose a continuous force contact model that accounts for energy dissipation during impact. The procedure is used for both rigid body and for nodal contact in the framework of flexible multibody dynamics.

Let the contact force between two bodies or a system component and an external object be a function of the pseudo-penetration δ and pseudo-velocity of penetration $\dot{\delta}$

$$\mathbf{f}_{s,i} = \left(K\delta^n + D\dot{\delta} \right) \ \mathbf{u} \tag{7}$$

where K is the equivalent stiffness, D is a damping coefficient and $\mathbf{u}$ is a unit vector normal to the impacting surfaces. The hysteresis dissipation is introduced in Eq. (7) by $D\dot{\delta}$ being the damping coefficient

$$D = \frac{3K\left(1-e^2\right)}{4\dot{\delta}^{(-)}}\delta^n \tag{8}$$

This coefficient is a function of the impact velocity $\dot{\delta}^{(-)}$, stiffness of the contacting surfaces and restitution coefficient e. For a fully elastic contact e=1 while for a fully plastic contact e=0. The generalized stiffness coefficient K depends on the geometry material properties of the surfaces in contact. For the contact between a sphere and a flat surface the stiffness is (Lankarani, 1995)

$$K = 0.424\sqrt{r}\left(\frac{1-v_i^2}{\pi E_i} + \frac{1-v_j^2}{\pi E_j}\right)^{-1} \tag{9}$$

where v_l and E_l are the Poisson's ratio and the Young's modulus associated to each surface and r is the radius of the impacting sphere. The nonlinear contact force is obtained by substituting Eq. (8) into Eq. (7)

$$\mathbf{f}_{s,i} = K \quad \delta^n \quad \left[1 + \frac{3\left(1-e^2\right)}{4}\frac{\dot{\delta}}{\dot{\delta}^{(-)}}\right] \ \mathbf{u} \tag{10}$$

This equation is valid for impact conditions, in which the contacting velocities are lower than the propagation speed of elastic waves, i.e., $\dot{\delta}^{(-)} \leq 10^{-5}\sqrt{E/\rho}$. Note also that other forms of this contact model can be devised for other materials and geometric conditions departing from the premises of the Hertzian elastic contact theory.

MULTIBODY DYNAMICS OF RAIL GUIDED VEHICLES

The multibody dynamics methodologies, independently of the formalisms used to describe their equations of motion, contain most of the ingredients required to describe complex systems. These methodologies also allow incorporating the equilibrium equations of other disciplines elegantly and efficiently. The study of rail guided vehicles in a wide range of situations is used here to demonstrate how contact problems can be handled either by using kinematic constraints or by developing appropriate continuous force contact laws even in cases of structural impact. Suitable forms for the description of the deformation of structures during vehicle impact are also presented, still in the framework of rigid multibody dynamics. The study of roller coaster dynamics, pantograph-catenary interaction, passenger train dynamics and train crashworthiness provide the cases with which such features of multibody dynamics are demonstrated.

Roller-coaster dynamics

The motion of the vehicles in a roller-coaster is completely guided along the rails. From this point of view this is not a classical contact problem but a problem of guidance of a vehicle over a prescribed track, which is introduced here as a kinematic constraint (Pombo and Ambrósio, 2003). The vehicle used in this work moves on a three-dimensional track with the geometry illustrated in Fig.3.
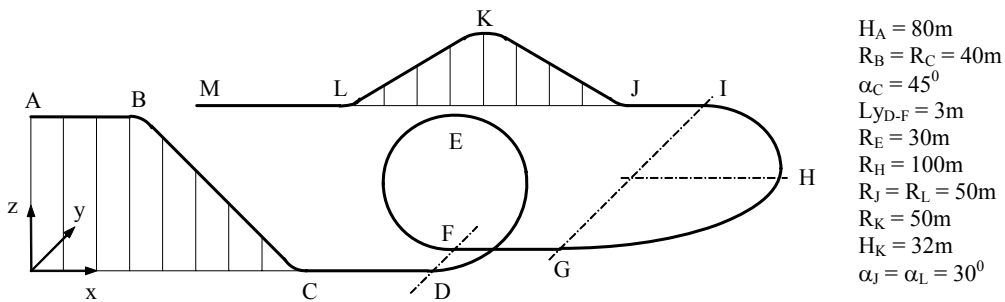

$H_A = 80m$
$R_B = R_C = 40m$
$\alpha_C = 45^0$
$Ly_{D-F} = 3m$
$R_E = 30m$
$R_H = 100m$
$R_J = R_L = 50m$
$R_K = 50m$
$H_K = 32m$
$\alpha_J = \alpha_L = 30^0$

Figure 3 – Roller coaster geometry

Prescribed Motion Constraint

The objective here is to define the constraint equations that enforce a certain point, of the given rigid body, to follow the reference path. Consider a point R, located on a rigid body i, that has to follow the specified path, as depicted in Fig. 4. The path is defined by a parametric curve $\mathbf{g}(L)$, which is controlled by a global parameter L that represents the length traveled by the point along the curve until the current location of point R. The kinematic constraint is written as:

$$\mathbf{\Phi}^{(pmc,3)} = \mathbf{0} \quad \equiv \quad \mathbf{r}_i^R - \mathbf{g}(L) = \mathbf{0} \tag{11}$$

where $\mathbf{r}_i^R = \mathbf{r}_i + \mathbf{A}_i \mathbf{s}'^R_i$ represents the coordinates of point R with respect to the global coordinate system (x,y,z), $\mathbf{r}_i$ is the vector that defines the location of the body-fixed coordinate system $(\xi,\eta,\zeta)_i$, $\mathbf{A}_i$ is the transformation matrix from the body i fixed coordinates to the global reference frame, and $\mathbf{s}'^R_i$ represents the coordinates of point R with respect to the body-fixed reference frame. The vector $\mathbf{g}(L)=\{x(L), y(L), z(L)\}^T$ represents the Cartesian coordinates of the curve where point R is constrained to move and L is the curve parametric variable. For notational purposes $(.)'$ means that $(.)$ is expressed in body-fixed coordinates. The constraint equations are assigned with a superscript of two indices, where the first denotes the type of constraint and the second defines the number of independent equations that it involves.
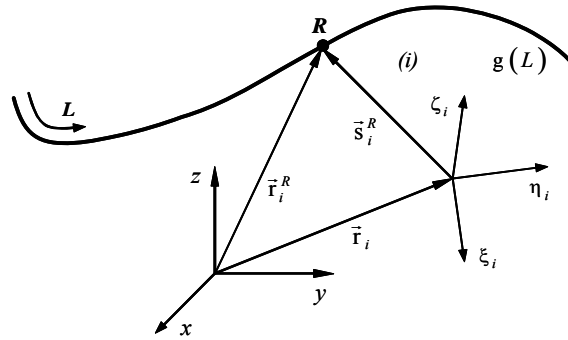

Figure 4 – Prescribed motion constraint

The velocity equation is obtained as the time derivative of Eq. (11), leading to:

$$\dot{\mathbf{\Phi}}^{(pmc,3)} = \mathbf{0} \quad \equiv \quad \dot{\mathbf{r}}_i^R - \dot{\mathbf{g}}(L) = \mathbf{0} \equiv \begin{bmatrix} \mathbf{I} & -\tilde{\mathbf{s}}_i^R \mathbf{A}_i & -\dfrac{d\mathbf{g}}{dL} \end{bmatrix} \begin{bmatrix} \dot{\mathbf{r}} \\ \boldsymbol{\omega}' \\ \dot{L} \end{bmatrix} = \mathbf{0} \tag{12}$$

The contribution of the prescribed motion constraint, Eq. (11) to the Jacobian matrix of the system is the 3×7 submatrix:

$$\mathbf{\Phi}_{\mathbf{q}}^{(pmc,3)} = \begin{bmatrix} \mathbf{I} & -\tilde{\mathbf{s}}_i^R \mathbf{A}_i & -\dfrac{d\mathbf{g}}{dL} \end{bmatrix} \tag{13}$$

in Eq. (13), $\mathbf{I}$ is a 3×3 identity matrix and $\mathbf{s}_i^R = \mathbf{A}_i \mathbf{s}'^R_i$ represents the coordinates of point R with respect to the $(\xi,\eta,\zeta)_i$ coordinate system, written in global coordinates.

The acceleration equation is obtained by the derivative of Eq. (13) with respect to time. The resulting equation is:

$$\ddot{\mathbf{\Phi}}^{(pmc,3)} = \mathbf{0} \quad \equiv \quad \begin{bmatrix} \mathbf{I} & -\tilde{\mathbf{s}}_i^R \mathbf{A}_i & -\dfrac{d\mathbf{g}}{dL} \end{bmatrix} \begin{bmatrix} \ddot{\mathbf{r}} \\ \dot{\boldsymbol{\omega}}' \\ \ddot{L} \end{bmatrix} = -\tilde{\boldsymbol{\omega}}_i \dot{\mathbf{s}}_i^R + \dfrac{d^2\mathbf{g}}{dL^2} \dot{L}^2 \tag{14}$$

where $\ddot{\mathbf{r}}_i = \{\ddot{x} \quad \ddot{y} \quad \ddot{z}\}^T_i$ are the translational accelerations of body i, $\dot{\boldsymbol{\omega}}'_i = \{\dot{\omega}_\xi \quad \dot{\omega}_\eta \quad \dot{\omega}_\zeta\}^T_i$ represent the angular accelerations of the body-fixed coordinate system $(\xi,\eta,\zeta)_i$, expressed in local coordinates, and $\ddot{L}$ is the second time derivative of the curve parametric variable. The contribution of the constraint for the right-hand-side of the accelerations equation is given by the 3×1 vector, written as:

$$\boldsymbol{\gamma}^{\#} = -\tilde{\boldsymbol{\omega}}_i \dot{\mathbf{s}}_i^R + \dfrac{d^2\mathbf{g}}{dL^2} \dot{L}^2 \tag{15}$$

Equations. (11), (13) and (15) are the quantities that must be implemented in the constraint module of the code.

Local Frames Alignment Constraint

The second part of the constraint ensures that the spatial orientation of body i remains unchanged with respect to the moving Frenet frame associated to the reference path curve, as represented in Fig. 5.
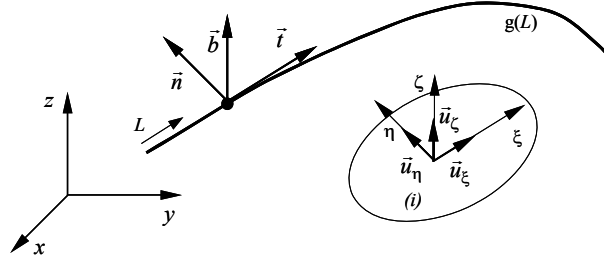

Figure 5 – Local frame alignment constraint

Consider a rigid body i where $(\mathbf{u}_\xi, \mathbf{u}_\eta, \mathbf{u}_\zeta)_i$ represent the unit vectors associated to the axis of the body-fixed coordinate system $(\xi, \eta, \zeta)_i$. Consider also that the Frenet frame of the general parametric curve $\mathbf{g}(L)$, is defined by the principal unit vectors $(\mathbf{t}, \mathbf{n}, \mathbf{b})_L$, as depicted in Fig. 5. Assume that, at the initial time of analysis, the relative orientation between the body vectors $(\mathbf{u}_\xi, \mathbf{u}_\eta, \mathbf{u}_\zeta)_i$ and the curve local frame $(\mathbf{t}, \mathbf{n}, \mathbf{b})_L$ are such that the following equations hold:

$$\mathbf{\Phi}^{(lfac,3)} = \mathbf{0} \quad \equiv \quad \begin{Bmatrix} \mathbf{n}^T \cdot \mathbf{u}_\xi \\ \mathbf{b}^T \cdot \mathbf{u}_\xi \\ \mathbf{n}^T \cdot \mathbf{u}_\zeta \end{Bmatrix} - \begin{Bmatrix} a \\ b \\ c \end{Bmatrix} = \mathbf{0} \tag{16}$$

The kinematic constraint ensures that this alignment will remain constant throughout the analysis. The transformation matrix from the body i fixed coordinates to the global coordinate system is written as:

$$\mathbf{A}_i = \begin{bmatrix} \mathbf{u}_\xi & \mathbf{u}_\eta & \mathbf{u}_\zeta \end{bmatrix}_i \tag{17}$$

With the purpose of having a more compact notation, let the following unit vectors be defined:

$$\mathbf{u}_1 = \{1 \quad 0 \quad 0\}^T \quad ; \quad \mathbf{u}_2 = \{0 \quad 1 \quad 0\}^T \quad ; \quad \mathbf{u}_3 = \{0 \quad 0 \quad 1\}^T \tag{18}$$

Equation (16) is now re-written as:

$$\mathbf{\Phi}^{(lfac,3)} = \mathbf{0} \quad \equiv \quad \begin{Bmatrix} \mathbf{n}^T \mathbf{A}_i \mathbf{u}_1 \\ \mathbf{b}^T \mathbf{A}_i \mathbf{u}_1 \\ \mathbf{n}^T \mathbf{A}_i \mathbf{u}_3 \end{Bmatrix} - \begin{Bmatrix} a \\ b \\ c \end{Bmatrix} = \mathbf{0} \tag{19}$$

The velocity equation for this constraint is obtained as the time derivative of Eq. (19), expressed as:

$$\dot{\mathbf{\Phi}}^{(lfac,3)} = \mathbf{0} \quad \equiv \quad \begin{bmatrix} \mathbf{0}^T & -\mathbf{n}^T \mathbf{A}_i \, \tilde{\mathbf{u}}_1 & \left(d\mathbf{n}/dL \right)^T \mathbf{A}_i \mathbf{u}_1 \\ \mathbf{0}^T & -\mathbf{b}^T \mathbf{A}_i \, \tilde{\mathbf{u}}_1 & \left(d\mathbf{b}/dL \right)^T \mathbf{A}_i \mathbf{u}_1 \\ \mathbf{0}^T & -\mathbf{n}^T \mathbf{A}_i \, \tilde{\mathbf{u}}_3 & \left(d\mathbf{n}/dL \right)^T \mathbf{A}_i \mathbf{u}_3 \end{bmatrix} \begin{bmatrix} \dot{\mathbf{r}} \\ \boldsymbol{\omega}' \\ \dot{L} \end{bmatrix} = \mathbf{0} \tag{20}$$

The contribution of the local frames alignment constraint (19) to the Jacobian matrix of the system is the 3×7 submatrix given by:

$$\mathbf{\Phi}_q^{(lfac,3)} = \begin{bmatrix} \mathbf{0}^T & -\mathbf{n}^T \mathbf{A}_i \, \tilde{\mathbf{u}}_1 & \left(d\mathbf{n}/dL \right)^T \mathbf{A}_i \mathbf{u}_1 \\ \mathbf{0}^T & -\mathbf{b}^T \mathbf{A}_i \, \tilde{\mathbf{u}}_1 & \left(d\mathbf{b}/dL \right)^T \mathbf{A}_i \mathbf{u}_1 \\ \mathbf{0}^T & -\mathbf{n}^T \mathbf{A}_i \, \tilde{\mathbf{u}}_3 & \left(d\mathbf{n}/dL \right)^T \mathbf{A}_i \mathbf{u}_3 \end{bmatrix} \tag{21}$$

Where $\mathbf{0}^T$ is a 1×3 null vector. The acceleration equation is the time derivative of Eq. (20) and it is written as:

$$\ddot{\boldsymbol{\Phi}}^{(lfac,3)} = \mathbf{0} \equiv \begin{bmatrix} \mathbf{0}^T & -\mathbf{n}^T \mathbf{A}_i \, \tilde{\mathbf{u}}_I & \left(d\mathbf{n}/dL\right)^T \mathbf{A}_i \, \mathbf{u}_I \\ \mathbf{0}^T & -\mathbf{b}^T \mathbf{A}_i \, \tilde{\mathbf{u}}_I & \left(d\mathbf{b}/dL\right)^T \mathbf{A}_i \, \mathbf{u}_I \\ \mathbf{0}^T & -\mathbf{n}^T \mathbf{A}_i \, \tilde{\mathbf{u}}_3 & \left(d\mathbf{n}/dL\right)^T \mathbf{A}_i \, \mathbf{u}_3 \end{bmatrix} \begin{bmatrix} \ddot{\mathbf{r}} \\ \dot{\boldsymbol{\omega}}' \\ \ddot{L} \end{bmatrix} =$$
$$-\left\{ \begin{array}{l} \left[2\dot{L} \left(d\mathbf{n}/dL\right)^T \mathbf{A}_i \, \tilde{\boldsymbol{\omega}}'_i + \mathbf{n}^T \mathbf{A}_i \, \tilde{\boldsymbol{\omega}}'_i \, \tilde{\boldsymbol{\omega}}'_i + \dot{L}^2 \left(d^2\mathbf{n}/dL^2\right)^T \mathbf{A}_i \right] \mathbf{u}_I \\ \left[2\dot{L} \left(d\mathbf{b}/dL\right)^T \mathbf{A}_i \, \tilde{\boldsymbol{\omega}}'_i + \mathbf{b}^T \mathbf{A}_i \, \tilde{\boldsymbol{\omega}}'_i \, \tilde{\boldsymbol{\omega}}'_i + \dot{L}^2 \left(d^2\mathbf{b}/dL^2\right)^T \mathbf{A}_i \right] \mathbf{u}_I \\ \left[2\dot{L} \left(d\mathbf{n}/dL\right)^T \mathbf{A}_i \, \tilde{\boldsymbol{\omega}}'_i + \mathbf{n}^T \mathbf{A}_i \, \tilde{\boldsymbol{\omega}}'_i \, \tilde{\boldsymbol{\omega}}'_i + \dot{L}^2 \left(d^2\mathbf{n}/dL^2\right)^T \mathbf{A}_i \right] \mathbf{u}_3 \end{array} \right\}$$

(22)

The contribution of the local frames alignment acceleration equation, described by Eq. (22) for the right-hand-side of the accelerations equation is given by the 3×1 vector, written as:

$$\gamma^{\#} = -\left\{ \begin{array}{l} \left[2\dot{L} \left(d\mathbf{n}/dL\right)^T \mathbf{A}_i \, \tilde{\boldsymbol{\omega}}'_i + \mathbf{n}^T \mathbf{A}_i \, \tilde{\boldsymbol{\omega}}'_i \, \tilde{\boldsymbol{\omega}}'_i + \dot{L}^2 \left(d^2\mathbf{n}/dL^2\right)^T \mathbf{A}_i \right] \mathbf{u}_I \\ \left[2\dot{L} \left(d\mathbf{b}/dL\right)^T \mathbf{A}_i \, \tilde{\boldsymbol{\omega}}'_i + \mathbf{b}^T \mathbf{A}_i \, \tilde{\boldsymbol{\omega}}'_i \, \tilde{\boldsymbol{\omega}}'_i + \dot{L}^2 \left(d^2\mathbf{b}/dL^2\right)^T \mathbf{A}_i \right] \mathbf{u}_I \\ \left[2\dot{L} \left(d\mathbf{n}/dL\right)^T \mathbf{A}_i \, \tilde{\boldsymbol{\omega}}'_i + \mathbf{n}^T \mathbf{A}_i \, \tilde{\boldsymbol{\omega}}'_i \, \tilde{\boldsymbol{\omega}}'_i + \dot{L}^2 \left(d^2\mathbf{n}/dL^2\right)^T \mathbf{A}_i \right] \mathbf{u}_3 \end{array} \right\}$$

(23)

The complete set of quantities that is necessary to implement computationally in the general spatial curve constraint is described by Eqs. (11), (13), (15), (19), (21) and (23). These quantities must be implemented in the constraint module of the computer code.

PRE-PROCESSOR for railway geometric description

For multibody analysis, the track models must be defined in the form of parameterized curves, being the parametrization in terms of shape preserving splines selected here (Pombo and Ambrósio, 2007). A pre-processor program uses these parametric descriptions in order to define the nominal geometry of the track centerline as function of the curve length parameter. This information is organized in a database where all quantities, necessary to define the spatial curve constraint, are obtained as a function of the track length, and measured from its origin. The formulation used by the railway pre-processor for the accurate description of the track geometry can be summarized as follows:
   a) The geometry of the track centerline can be parameterized using piecewise cubic interpolation. Here, the user only has to define a set of control points that are representative of the railway geometry as well as the correspondent cant angle at each point.
   b) Regardless the approach used to describe the railway geometry, the track centerline is parameterized as function of the track length.
   c) The track cant angle is also parameterized as function of the track length and the principal unit vectors, which define the Frenet frames associated to the track centerline after the cant angle rotation, are calculated.
   d) An output database for the railway model is created and all parameters necessary to define the geometric characteristics of the track centerline are stored in it. Each database has a track length step as small as desired by the user. During dynamic analysis the railway database is used by the multibody code that performs linear interpolation on the points contained in the table in order to find the necessary geometric information at each time step.

In the computational implementation of the prescribed motion constraint all quantities required in Eqs. (11) through (23) are obtained by a linear interpolation of the railway database defined in Fig. 6. Therefore, the stepping parameter used to build the database must be of the same order of the product of the integration time step by the vehicle velocity.

Application to the study of a roller-coaster vehicle

In Fig. 4 a view of the roller coaster, as used in the application, is presented. In this figure, H_i refers to the height of the point i, R_j designates the radius of curve segment j, α_k is the angle that each track segment k makes with the horizontal plane and Ly_{i-j} refers to the distance between two points i and j. The roller coaster model is assembled considering transition curves with 60 m length for the connections between the horizontal curve G–I and the straight segments F–G and I–J. The cant angle for the circular curve G–I is −1.014 rad (−58.1°) and it varies linearly in each of the transition segments. The track cant angle adopted corresponds to the equilibrium cant, i.e., the cant for zero track plane acceleration.
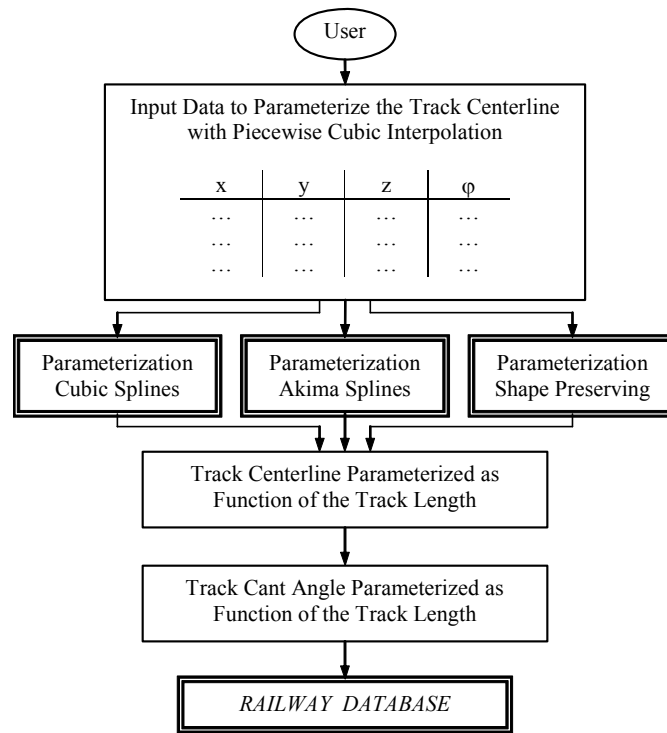
Figure 6 –Schematic representation of railway pre-processor

The roller coaster vehicle consists of a train with three cars that are interconnected by linking bars, as represented in Fig. 7. The multibody model of the vehicle is assembled using eleven rigid bodies, identified with the numbers 1 to 11, corresponding to 3 carbodies, 6 wheelsets and 2 linking bars. The origin of the global coordinate system (x,y,z) is located at the height of the track surface, as depicted in Fig. 7. The train is assembled in such a manner that the rear wheelset center is placed on the origin of the x axis.
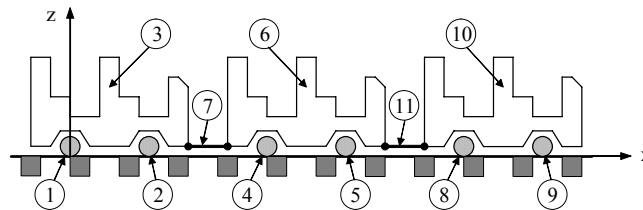
Figure 7 – Multibody model of the roller coaster vehicle

A local reference frame (ξ,η,ζ) is rigidly attached to the centre of mass (CM) of each body. The spatial orientations of these reference frames are such that they are aligned with the principal inertia directions of the respective rigid body. The initial position of each rigid body is given by the location of its CM with respect to the global reference frame (x,y,z). The mass, the inertia properties with respect to the three principal axes and the initial position of each rigid body are presented reference (Pombo and Ambrósio, 2007).

Four spherical joints are used in the roller coaster vehicle model to connect the linking bars to the carbodies in order to assemble the train. Each spherical joint imposes three kinematic constraints between the two connected bodies in order to control their relative motion, allowing. Six general spatial curve kinematic constraints are used to assemble the multibody model of the roller coaster vehicle. These kinematic constraints are defined between the vehicle wheelsets and the track centerline in order to enforce the wheelsets to move along the roller coaster track, being their spatial orientation prescribed according to the track geometry. The type of kinematic constraints used to assemble the roller coaster vehicle model, the bodies connected by them and the local coordinates of the attachment points are presented reference (Pombo and Ambrósio, 2007).

The suspension of the roller coaster vehicle consists of a group of flexible links that ensure the transmission of forces between the carbodies and the wheelsets. Here, the model used for the suspension of each car consists on a three-dimensional spring element, assembled at each wheelset extremity, which connects the wheelsets to the carbody, as shown in Fig. 8. The model also uses four vertical dampers, assembled between the wheelsets and the carbody. The characteristics of these spring and damper elements, the identification of the bodies connected by them and the local coordinates of their attachment points, are presented in (Pombo and Ambrósio, 2007) for a representative car of the roller coaster vehicle.
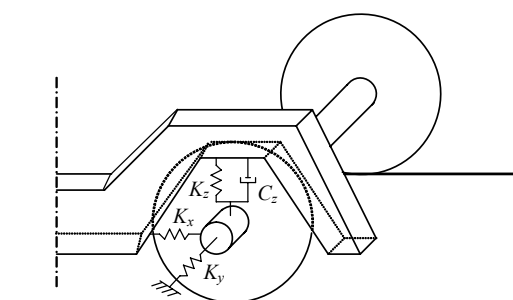
Figure 8 – Schematic representation of the suspension model used in each roller coaster car

The acceleration perceived by a passenger traveling in the roller coaster vehicle is illustrated in Fig. 9. It represents the acceleration in *z* direction in the carbody of the rear car, for both track models parameterized with cubic and shape preserving splines and for a distance between control points of 1 m. During the simulation, the two small peaks observed in the vertical acceleration, at 35 and 40 seconds, are obtained when the vehicle passes through the horizontal transition curves where the track cant angle has a linear variation.
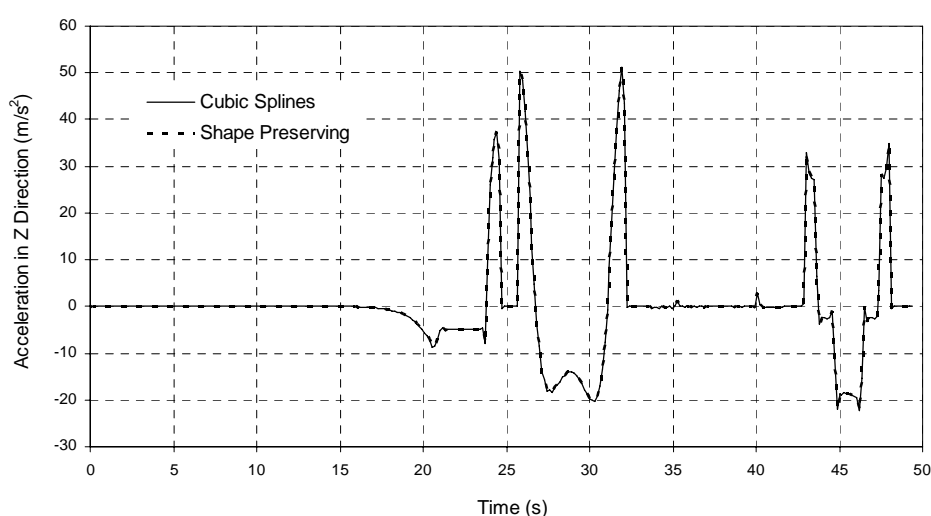
Figure 9 – Rear car acceleration in *z* direction for distances between control points of 1 m

One of the important features of the methodology now proposed is its ability to calculate the reaction forces that develop between the track and the vehicle wheelsets. Figure 10 represents the vertical reaction forces on the wheelsets of the rear roller coaster car. These results are obtained for a track model parameterized with shape preserving splines.
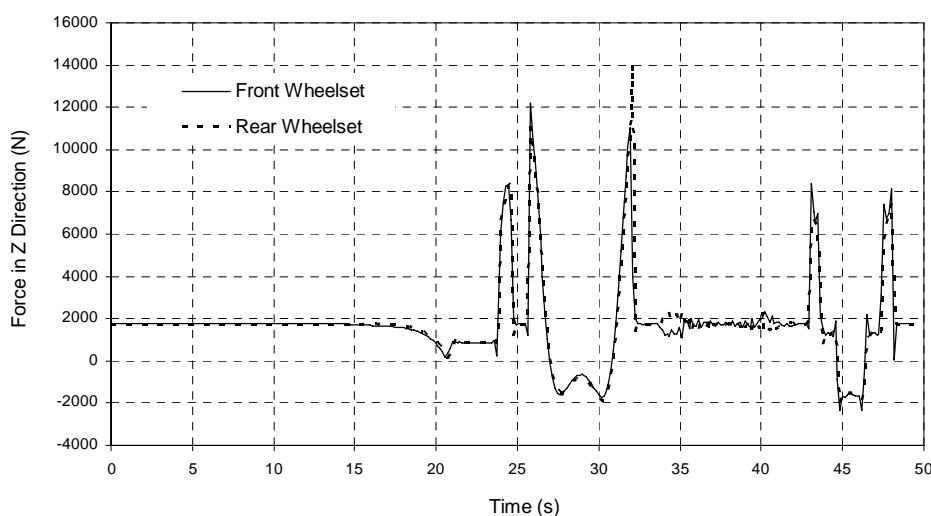
Figure 10 – Vertical reaction forces that develop between the track and the wheelsets of the rear car.

The large peaks of vertical reaction forces observed in Fig. 10 result from the changes of the vertical curvature between parts of the track with different geometric characteristics, being some of the transition points shown in the pictures presented in Fig. 11. These large vertical loads on the roller coaster track reflect the fact that no vertical transition curves are used in the track model. Note also the correlation between the results presented in this figure and the rear wheelset accelerations in Fig. 9.
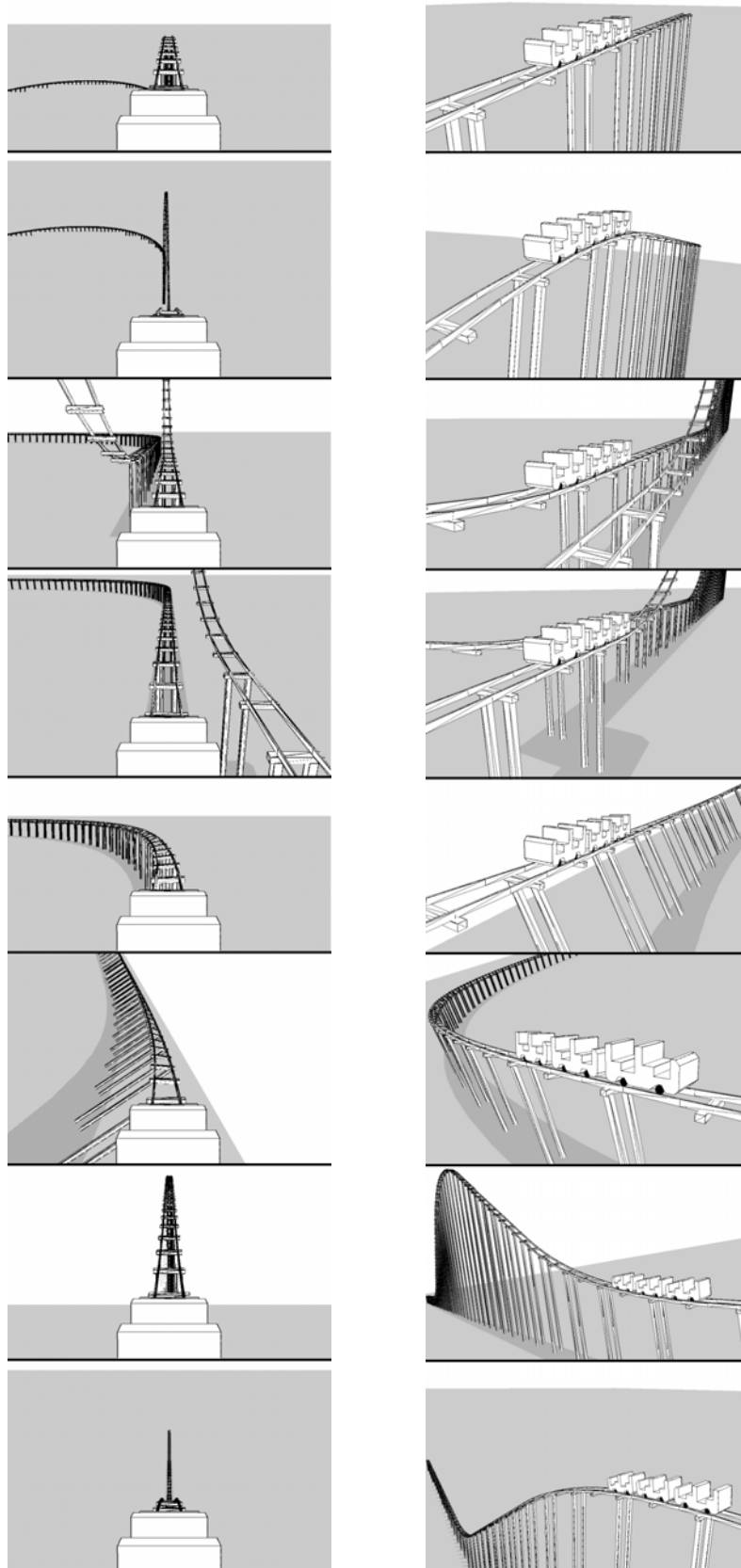

Figure 11 – Views of the roller coaster motion resulting from the dynamic analysis

Pantograph-catenary interaction analysis

The pantograph-catenary system is still today the most reliable form of collecting electric energy for running trains, when high speed operational conditions are considered. This system should ideally run with relatively low contact forces, in order to minimize wear and damage of the contacting elements of the system, and no contact loss should be observed, so that the power supply would be constant and no electric arching would be observed. Therefore, the study of this problem involves the representation of the contact between the pantograph registration strips and the catenary over-head line in which the pantograph and rail vehicle are modeled as multibody systems and the overhead line is modeled using finite elements. This study also exemplifies how the multibody system can be co-simulated with other models that use different formalisms, such as the finite element method in this case (Rauter et al., 2007).

Pantograph modeling issues

In general, a pantograph consists of a collection of bodies and mechanical elements, as depicted in Fig. 12, attached to a railway carbody that is moving along the track. The contact between the pantograph and the catenary occurs in the registration strips, represented as bodies 2 and 3 in Fig. 12.
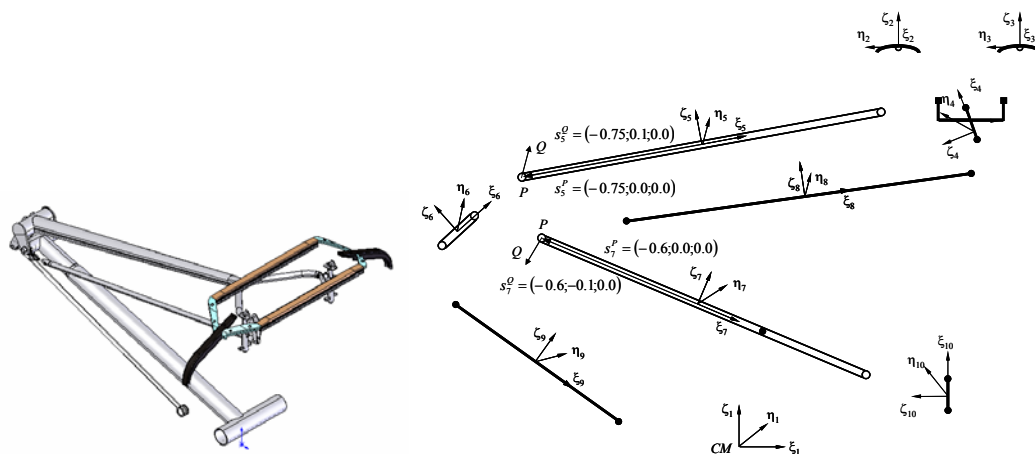
Figure 12 Pantograph represented as a multibody system.

Although the moving components of the pantograph have some level of flexibility in this model they are represented as rigid bodies. Deformable elements, such as springs and dampers, are used to model relevant internal forces that represent interactions between rigid bodies of the system. In existent pantographs a good number of non-linear elements differ from standard kinematic and compliance elements used in traditional mechanical systems, as those exemplified in Fig. 13. There are different types of force elements that do not have a linear type behavior in the pantograph model. Among these, some relevant force elements, as that represented in Fig. 13, include friction effects besides the elastic forces and the damping.
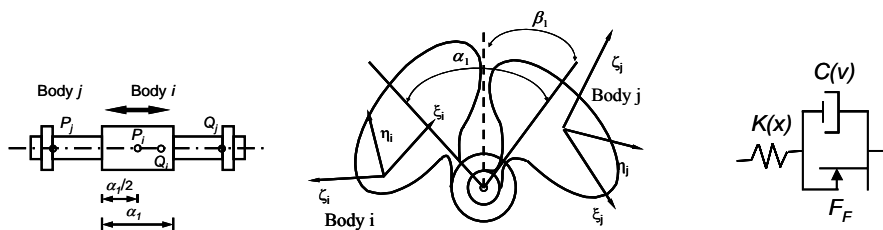

Figure 13 Revolute and translational joints geometric operational limits and force elements used for the pantograph model.

The strategy used to define the reference motion of the pantograph consists in specifying the kinematics of the pantograph base using the prescribed motion constraint, as implied by Fig. 14. The motion of the pantograph must be compatible with the geometry of the catenary.
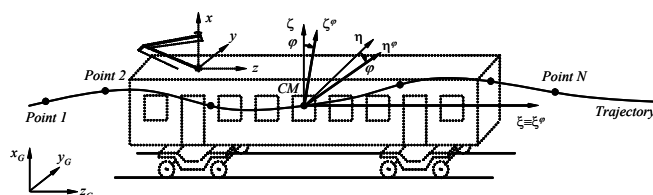

Figure 14 Prescribed motion constraint of the carbody

Catenary modeling issues

Catenaries are complex periodical structures, as that represented in Fig. 15. Examples of typical structural elements involved in the catenary model are the contact, stitch and messenger wires, droppers and registration arms. Depending on the catenary systems there are other elements that may have to be considered. In any case, the contact wire is the responsible for the contact between catenary and pantograph and therefore the element that provides electrical power. The messenger wire prevents excessive sag caused by the contact wire weight. Both of these wires are connected by vertical, tensile force droppers. The finite element method is preferred to build models of complex catenary systems. In the FE code used here, for the dynamic analysis of the catenary, the main catenary elements, contact and messenger wires are modeled by using pre-tensioned Euler-Bernoulli beam elements.
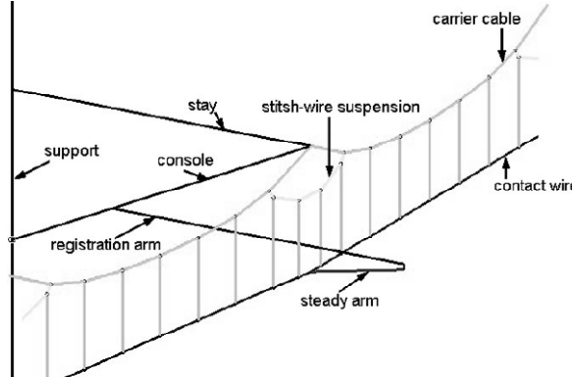
Figure 15 Catenary three-dimensional mesh in the Finite Element software EUROPACAS

A typical catenary is characterized by having nonlinear type of behavior. For example the stiffness of the messenger and contact wires is dependent of its current deformation state and the droppers have high tensile stiffness, but no resistance to compression. The overall vertical stiffness of the catenary is function of the behavior of each of its elements. Furthermore, the contact loss with the pantograph introduces also nonlinear effects on the behavior of the catenary.

The pantograph and catenary systems are related due to the interaction between the registration strips of the pantograph and the contact wires of the catenary. The contact force due to pantograph-catenary interaction, regarding present operating conditions and pantograph and catenary technology, is characterized by a low-frequency oscillating force with high relative amplitude. Railway industry measurement data shows that reasonable values for the contact force are, for a train running at approximately 80 m/s: a mean value of 200N oscillating between 300N and 100N. Loss of contact in particular points of the catenary may also occur.

Integration of the catenary finite element equations of motion

The integration of the catenary finite element model requires the use of an integrator of the Newmark family (Hughes, 1987). At any given time step the algorithm proceeds by first predicting the displacements $\tilde{\mathbf{d}}_{t+\Delta t}$ and velocities $\tilde{\mathbf{v}}_{t+\Delta t}$ for the new time step by using the information of the last completed time step as

$$\tilde{\mathbf{d}}_{t+\Delta t} = \mathbf{d}_t + \Delta t\, \mathbf{v}_t + \frac{\Delta t^2}{2}\left(1-2\beta\right)\mathbf{a}_t$$
$$\tilde{\mathbf{v}}_{t+\Delta t} = \mathbf{v}_t + \Delta t\left(1-\gamma\right)\mathbf{a}_t \tag{24}$$

where $\gamma=1/2$ and $\beta=1/4$ for the trapedoizal rule. Based on the position and velocity predictions for the finite element mesh and on the pantograph predicted position and velocity the contact forces are evaluated for $t+\Delta t$ and the finite element mesh accelerations are calculated from the equilibrium equation

$$\left(\mathbf{M} + \gamma\,\Delta t\,\mathbf{C} + \beta\,\Delta t^2\mathbf{K}\right)\mathbf{a}_{t+\Delta t} = \mathbf{f}_{t+\Delta t} - \mathbf{C}\tilde{\mathbf{v}}_{t+\Delta t} - \mathbf{K}\tilde{\mathbf{d}}_{t+\Delta t} \tag{25}$$

Then, with the acceleration $\mathbf{a}_{t+\Delta t}$ the positions and velocities of the finite elements at time $t+\Delta t$ are corrected by

$$\mathbf{d}_{t+\Delta t} = \tilde{\mathbf{d}}_{t+\Delta t} + \beta\,\Delta t^2\mathbf{a}_{t+\Delta t}$$
$$\mathbf{v}_{t+\Delta t} = \tilde{\mathbf{v}}_{t+\Delta t} + \gamma\,\Delta t\,\mathbf{a}_{t+\Delta t} \tag{26}$$

These procedure is repeated until a stability value is reached for a given time step.

Integration of the pantograph multibody equations of motion

The integration of the pantograph multibody model, exemplified in Fig. 2, generally use variable time step and order integrator algorithms (Petzold, 1984). In this work the multibody code uses a Gear multi-step multi-order integration algorithm, as reported by Shampine and Gordon (1975) and by Gear (1971). For a given time step it is necessary to know the forces, including the contact forces due to the pantograph-catenary interaction, before the accelerations are calculated, for both predictive and corrective integration steps. Contrary to the Newmark algorithms used for the finite element model of the catenary where only the time response of the system during the current time step is required the time integration algorithm used for the multibody model uses the previous response of the system to improve the predictive capabilities for the forward response. Therefore, at a given time step the information available for the catenary and for the pantograph may not be sufficient to calculate the contact forces as it is. A co-simulation formalism must be devised to handle this situation.

Co-simulation between the pantograph and catenary multibody codes

The analysis of the pantograph-catenary interaction is done through two independent codes, the pantograph code, developed using the multibody methodology reported in this work, and the catenary code, developed using a finite element methodology. Both of these programs can work as being stand-alone. The structure of the communication scheme is shown in Fig. 16. The MB code provides the FEM code with the position and velocity of the pantograph's registration strip. The FEM code calculates the contact force, using the contact model represented by Eq. (10), and its application points in the pantograph and catenary, using a geometric interference model. These forces are applied to the catenary, in the finite element code, and to the pantograph model, in the MB code. Each code integrates separately the equations of motion of each sub-system based on the shared force information.
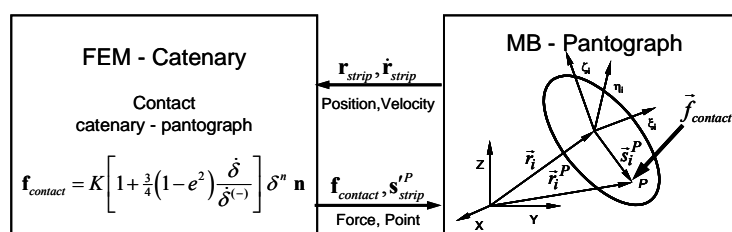

Figure 16 Structure of the communication scheme between the MB code and the FEM code

Therefore the FEM code needs a prediction of the positions and velocities not only of the catenary but also of the pantograph in a forthcoming time before advancing to a new time step. A predicted contact force is calculated and, using the finite element method equations of equilibrium, the catenary accelerations are computed for the new time-step. The calculated acceleration values are used to correct the initially predicted positions and velocities of the catenary. To proceed with the dynamic analysis, the MB code needs information about the positions and velocities of the pantograph components and also the contact force and its application point coordinates at different time instants during the integration time period, and not only at its start and end. The compatibility between the two integration algorithms imposes that the state variables of the two subsystems are readily available during the integration time but also that a reliable prediction of the contact forces is also available at any given time step. The key of the synchronization procedure between the MB and FE codes is the time integration, as depicted by Fig. 17. The communication must ensure the correct dynamic analysis of the pantograph-catenary system, including the loss and regain of contact.

Analysis results

The model of the catenary used in this work, pictured in Fig. 15, corresponds to the Paris-Lyon French high speed railway track. All the structural elements that compose the real catenary are modeled including the contact, messenger and stitch wires, droppers, registration and steady arms. The catenary static state (displacements, forces), which is a very sensitive parameter, is computed using a non-linear strategy since the wires' stiffness depends on their actual displacements. The pantograph-catenary coupling can then be considered. In Fig. 18 the numerical results of the model described are shown together with experimentally measured values of the pantograph-catenary system used in the same high speed line. The velocity of the pantograph on the catenary corresponds to a 80 m·s^{-1} moving train.

The correlation of the numerical and experimental results, according to the EN50318 standard (filtered at 20 Hz), are satisfactory, especially considering that no aerodynamic effects, cross-wind or railway dynamics perturbations are considered in the simulation. The filtered results include the effects of the structural elements of the catenary, due to the passage of the pantograph, but may not include, for example, the effects of singular defects. The experimental data was obtained over a commercial high-speed catenary in operating conditions, and therefore subjected to climatic defects, wear and other general defects. Regardless of these differences the results show that the model developed and the methodology applied are suitable to describe the pantograph catenary contact. More developments of this methodology and its application to a wide number of pantographs and catenaries for different operating conditions, with and without defects, are considered in the European Project EUROPAC, in the framework of which the methodologies now presented have been developed.
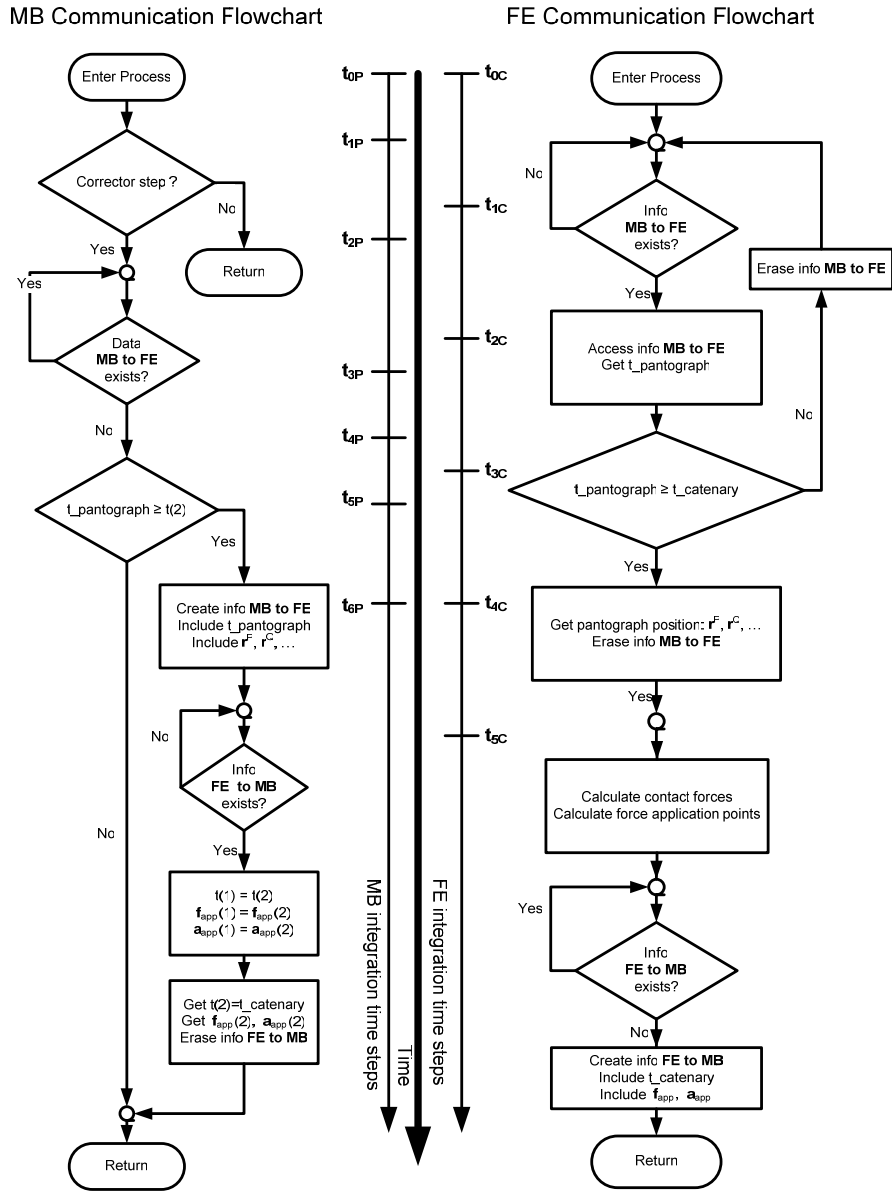
MB Communication Flowchart

FE Communication Flowchart

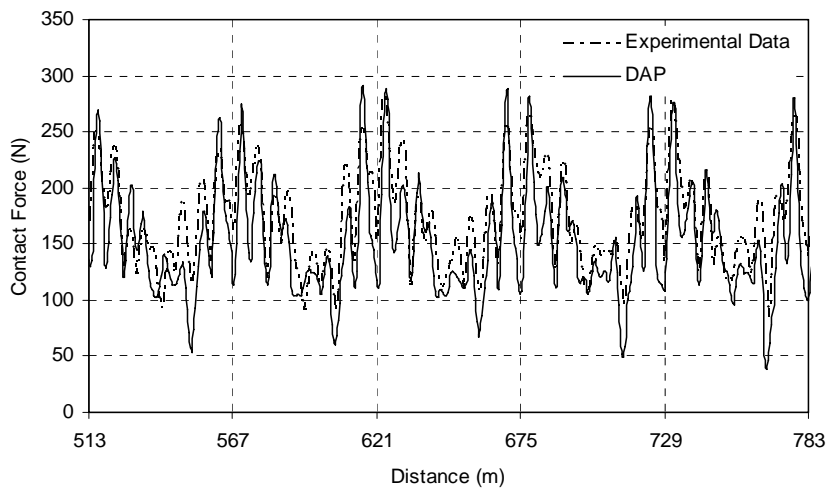**Figure 17 - Flowchart of the communication procedure between the MB and FE codes.**

Figure 18 - Numerical (solid) and experimental measurements (dashed) in a French high speed line, for a train speed of 80 m·s⁻¹

Railway dynamics

One of the interesting applications of multibody dynamics with contact mechanics is the description of the wheel-rail contact in railway dynamics. The stability of the running vehicle depends ultimately in the rail-wheel contact and in the vehicle primary suspension. Therefore, methodologies that provide accurate models to represent the phenomena are of particular importance. In a general case of a railway vehicle one or two points of each wheel are in contact with the rail, as shown in Fig. 19. The diametric section that contains the wheel flange contact point makes an angle s^f_{Rw} with the diametric section that contains the wheel tread contact point. The possibility of detecting contact in different diametric sections allows predicting derailment and it is, therefore, of utmost importance.
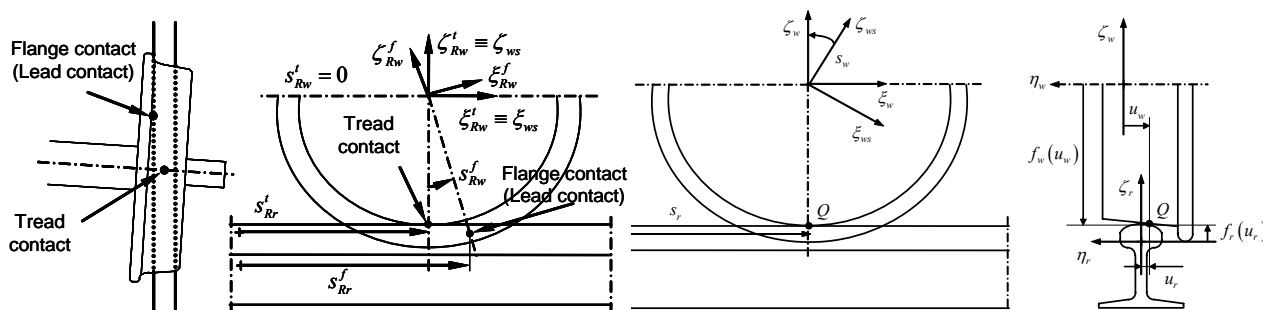
Figure 19 – Parameters defining the rail and wheel positions including the two points of contact possibility.

The contact model used to solve the problem of the wheel-rail interaction requires the definition of the geometry of the contacting surfaces in a parametric form. This needs to be general in the sense that the parametric equations must be able to represent any spatial configuration of the wheelsets and rails as well as any wheel and rail profiles obtained by direct measurements or by design requirements. This can be a difficult task, especially when the surfaces are not given by simple analytical functions. The approach followed here is to consider the surfaces of the wheels and rails as sweep surfaces obtained by dragging plane curves on spatial curves. As a result, the problem of describing the surface reduces to the problem of defining plane curves, which are the cross sections of the wheel and rail.

In the formulation developed for the contact between a rigid wheel and a rigid rail, four independent surface parameters are used to define the geometry of the surfaces in contact. The surface parameters s_r and u_r are used to describe the geometry of the rail surface, while s_w and u_w are the surface parameters used to define the wheel surface, as shown in Fig. 19 (Pombo and Ambrósio, 2004). The position vector of a contact point Q in the body coordinate system of the wheel or rail is a function of the surface parameters only. Such position vectors are defined as:

$$\mathbf{u}_l = \mathbf{u}_l\left(s_l , u_l\right) \quad ; \quad l = r,w \tag{27}$$

In all that follows the quantities with subscripts $(.)_r$ and $(.)_w$ refer to the rail and to the wheel, respectively, whereas the quantities with subscript $(.)_{ws}$ refer to the wheelset.

Rail surfaces in a general track

In order to account for any possible scenarios, such as a variation in the gauge or relative displacements and/or rotations of the rails due to the track irregularities, it is necessary to define the surface of each rail independently. Fig. 20 shows the left and right rails with an arbitrary geometry and surface profiles. The surface of each rail can be obtained as the envelope of the surfaces generated by the two-dimensional curve that defines the rail profile when it is moved along the rail space curve. In what follows quantities with subscripts $(.)_{Lr}$ and $(.)_{Rr}$ refer to left and right rails, respectively.
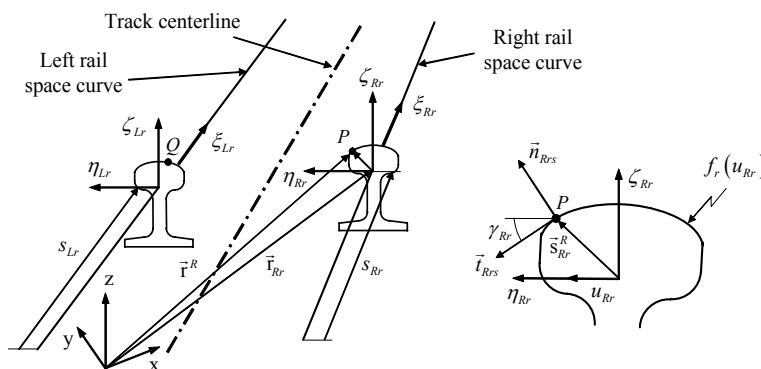

Figure 20 - Parameterization of the rail surface

In a general case, the surface geometry of the rail is described using the two surface parameters s_r and u_r. The arc length of the rail space curve, denoted by s_r, defines the rail cross-section on which the contact point lies. The parameter u_r defines the lateral position of the contact point in the rail profile coordinate system (ξ_r, η_r, ζ_r). Furthermore, u_r is used to define the rail profile curve at each cross section, as shown in Fig. 20. Assume that the right rail has a contact point P with one of the wheels. The right profile coordinate system $(\xi_{Rr}, \eta_{Rr}, \zeta_{Rr})$ of this contact is shown in Fig. 20. This frame translates along the right rail space curve and rotates about its origin. The location of the profile coordinate system along the space curve is defined such that the contact point P always lies in the (η_{Rr}, ζ_{Rr}) plane.

The location of the origin and the orientation of the right rail profile coordinate system, defined respectively by the vector $\mathbf{r}_{Rr}$ and the transformation matrix $\mathbf{A}_{Rr}$, are uniquely determined using the surface parameter s_r. Using this description, the global position vector of an arbitrary point P on the rail surface is written as:

$$\mathbf{r}^P = \mathbf{r}_{Rr} + \mathbf{A}_{Rr}\, \mathbf{s}'^{P}_{Rr} \tag{28}$$

where $\mathbf{s}'^{P}_{Rr}$ is the local position vector that defines the location of the contact point P on the rail surface with respect to the profile coordinate system. Note that due to the above-mentioned description of the rail geometry, the following relations hold:

$$\mathbf{r}_{Rr} = \mathbf{r}_{Rr}(s_{Rr}) \quad ; \quad \mathbf{A}_{Rr} = \mathbf{A}_{Rr}(s_{Rr}) \quad ; \quad \mathbf{s}'^{P}_{Rr} = \left\{\, 0 \quad u_{Rr} \quad f_r(u_{Rr}) \,\right\}^T \tag{29}$$

where f_r is the function that defines the rail profile. The transformation matrix $\mathbf{A}_{Rr}$ can be expressed in terms of the three unit vectors $\mathbf{t}_{Rr}$, $\mathbf{n}_{Rr}$ and $\mathbf{b}_{Rr}$ that define the moving reference frame associated to the right rail space curve. Hence, the transformation matrix is:

$$\mathbf{A}_{Rr} = \mathbf{A}_{Rr}(s_{Rr}) = \left[\, \mathbf{t}_{Rr}(s_{Rr}) \quad \mathbf{n}_{Rr}(s_{Rr}) \quad \mathbf{b}_{Rr}(s_{Rr}) \,\right] \tag{30}$$

The unit vectors are expressed uniquely in terms of the rail arc length, i.e., as function of the surface parameter s_{Rr}. The Cartesian components of these vectors are obtained from the respective rail database previously described.

Generally, in railway applications, the function f_r, which defines the rail profile at each cross section, is not given by simple analytical functions. It is proposed here that the rail profile is parameterized as function of the surface parameter u_r using a piecewise cubic interpolation scheme, in particular shape preserving splines (Irvine et al., 1986). Hence, to obtain $f_r(u_r)$ the user only has to define a set of control points that are representative of the rail profile geometry, as shown in Fig. 21. Note that this methodology is general as it allows performing the dynamic analysis of railway vehicles using rail profiles obtained from direct measurements or by design requirements.
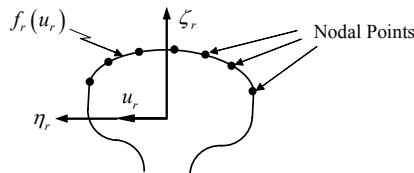

Figure 21 - Rail profile parameterization using piecewise cubic interpolation schemes

The multibody contact model used to solve the problem of wheel-rail contact requires the definition of the normal vector to the rail surface $\mathbf{n}_{rs}$ at the point of contact. For the right rail this normal vector is defined as:

$$\mathbf{n}_{Rrs} = \mathbf{A}_{Rr}\, \mathbf{n}'_{Rrs} \tag{31}$$

where $\mathbf{n}'_{Rrs} = \left\{ 0\,, \ -\sin\gamma_{Rrs}\,, \ \cos\gamma_{Rrs} \right\}^T$ is the unit normal vector to the right rail surface defined in the profile coordinate system $(\xi_{Rr}, \eta_{Rr}, \zeta_{Rr})$. This vector is obtained through the contact angle γ_{Rs}, measured in the cross-sectional plane, defined between the vector tangent to the right rail surface $\vec{t}_{Rrs}$, at the contact point, and the local axis η_{Rr}, as shown in Fig. 20. The contact angle is obtained by differentiating the function f_r, which defines the rail profile, with respect to the non-generalized surface parameter u_r associated to the right rail, as:

$$\gamma_{Rrs} = \mathrm{tg}^{-1}\left(\frac{df_r(u_{Rr})}{du_{Rr}} \right) \tag{32}$$

In all that follows, the quantities with subscript $(.)_{Lrs}$ refer to the left rail surface whereas the quantities with subscript $(.)_{Rrs}$ refer to the right rail surface. Note that the locations of the profiles coordinate systems $(\xi_{Rr}, \eta_{Rr}, \zeta_{Rr})$ and $(\xi_{Lr}, \eta_{Lr}, \zeta_{Lr})$ are, respectively, given by the coordinates s_{Rr} and s_{Lr} measured on right and left space curves.

General wheel surface

To account for any spatial configuration of the wheelset and any wheel profile, which can be obtained from direct measurements, it is necessary to define the surface of each wheel independently. Figure 22 shows the left and right wheels assembled in a wheelset and with arbitrary surface profiles. The surface of revolution of each wheel is obtained as the envelope of the surfaces generated by a complete rotation, about the wheel axis, of the two-dimensional curve that defines the wheel profile. The quantities with subscripts $(.)_{Lw}$ and $(.)_{Rw}$ refer to the left and right wheels, respectively.
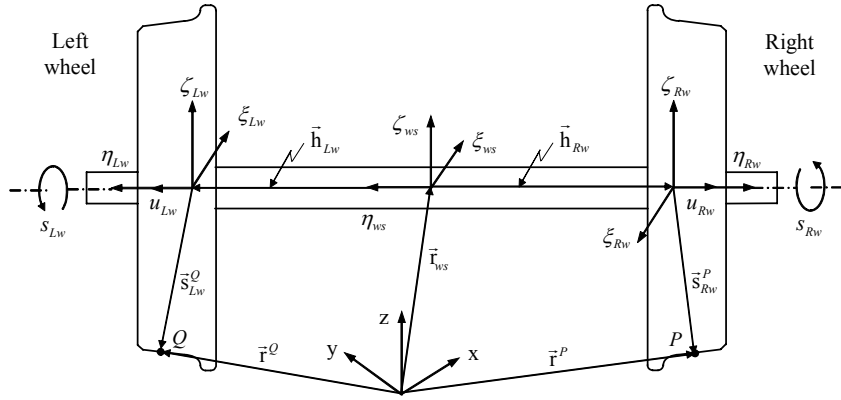
Figure 22 - Parameterization of the wheel surface

The surface geometry of the wheel is described using the two parameters. The surface parameter s_w represents the rotation of the wheel profile coordinate system (ξ_w, η_w, ζ_w) with respect to the wheelset coordinate system $(\xi_{ws}, \eta_{ws}, \zeta_{ws})$. The parameter u_w defines the lateral position of the contact point in the wheel profile coordinate system, i.e., represents the coordinate of vector $\mathbf{s}'_w$ on the wheel reference axis η_w, as shown in Fig. 22. Note that u_w also characterizes the wheel profile curve at each cross section. On each wheel, a profile coordinate system is defined by identifying the orientation of the cross section where the contact point is located. Assume that the left wheel has a contact point Q and the right wheel has a contact point P. These frames rotate about the wheel axis with respect to the wheelset coordinate system in such a way that the contact points Q and P always lie in the (η_{Lw}, ζ_{Lw}) and (η_{Rw}, ζ_{Rw}) planes respectively.

The origin and the orientation of the wheelset reference frame $(\xi_{ws}, \eta_{ws}, \zeta_{ws})$ are defined, respectively, by vector $\mathbf{r}_{ws}$ and transformation matrix $\mathbf{A}_{ws}$. The global positions of points on the surface of the left and right wheels are:

$$
\begin{aligned}
\mathbf{r}_{Lw}^{Q} &= \mathbf{r}_{ws} + \mathbf{s}_{ws}^{Q} = \mathbf{r}_{ws} + \mathbf{A}_{ws}\, \mathbf{s}_{ws}'^{Q} = \mathbf{r}_{ws} + \mathbf{A}_{ws}\left(\mathbf{h}_{Lw} + \mathbf{A}_{Lw}\, \mathbf{s}_{Lw}'^{Q}\right) \\
\mathbf{r}_{Rw}^{P} &= \mathbf{r}_{ws} + \mathbf{s}_{ws}^{P} = \mathbf{r}_{ws} + \mathbf{A}_{ws}\, \mathbf{s}_{ws}'^{P} = \mathbf{r}_{ws} + \mathbf{A}_{ws}\left(\mathbf{h}_{Rw} + \mathbf{A}_{Rw}\, \mathbf{s}_{Rw}'^{P}\right)
\end{aligned}
\tag{33}
$$

where and $\mathbf{h}_{Rw}$ are local position vectors that define the location of left and right wheels profiles coordinate systems with respect to the wheelset reference frame, given by:

$$
\mathbf{h}_{Lw} = \left\{0 \quad \tfrac{1}{2}H \quad 0\right\}^{T} \quad ; \quad \mathbf{h}_{Rw} = \left\{0 \quad -\tfrac{1}{2}H \quad 0\right\}^{T}
\tag{34}
$$

where H is the lateral distance between wheel profile origins. $\mathbf{A}_{Lw}$ and $\mathbf{A}_{Rw}$, in equation (33), are the transformation matrices from the left and right wheels coordinate systems to the wheelset reference frame

$$
\mathbf{A}_{Lw} = \begin{bmatrix} \cos s_{Lw} & 0 & \sin s_{Lw} \\ 0 & 1 & 0 \\ -\sin s_{Lw} & 0 & \cos s_{Lw} \end{bmatrix} \quad ; \quad \mathbf{A}_{Rw} = \begin{bmatrix} -\cos s_{Rw} & 0 & -\sin s_{Rw} \\ 0 & -1 & 0 \\ -\sin s_{Rw} & 0 & \cos s_{Rw} \end{bmatrix}
\tag{35}
$$

and $\mathbf{s}_{Lw}'^{Q}$ and $\mathbf{s}_{Rw}'^{P}$ are the local position vectors that define the location of the contact points Q and P on the wheel surfaces with respect to the profiles coordinate systems, respectively, as:

$$
\mathbf{s}_{Lw}'^{Q} = \left\{0 \quad u_{Lw} \quad f_w\left(u_{Lw}\right)\right\}^{T} \quad ; \quad \mathbf{s}_{Rw}'^{P} = \left\{0 \quad u_{Rw} \quad f_w\left(u_{Rw}\right)\right\}^{T}
\tag{36}
$$

where f_w is the function that defines the wheel profile. Generally in railway applications, the function f_w, which defines the wheel profile, is not given by simple analytical functions. In this investigation, it is proposed that the wheel profile is parameterized as a function of the surface parameter u_w using a piecewise cubic interpolation scheme, as described for the rail surface. Hence, to obtain $f_w(u_w)$ the user only has to define a set of control points that are representative of the profile geometry of the wheel tread and wheel flange, as shown in Fig. 23(a). Note that this procedure permits the dynamic analysis of railway vehicles using wheel profiles obtained from direct measurements or by design requirements.
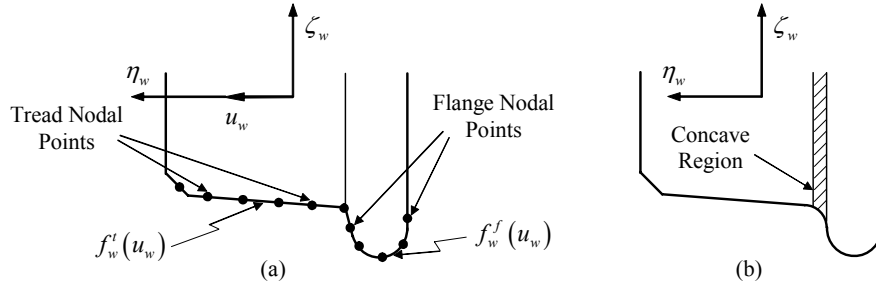
Figure 23 - Wheel profile: a) Parameterization using cubic interpolation schemes; b) Concave region

In the multibody contact model used to solve the problem of wheel-rail contact, it is necessary to devise a strategy to determine the location of the contact points between the parametric surfaces. The formulation proposed here requires that the parametric surfaces are convex. Therefore, when parameterizing the wheel profile, it is necessary to avoid the geometric description of the small concave region in the transition between the wheel tread and the wheel flange, which is depicted in Fig. 23(b). The wheel profile is represented by two independent functions f^t_w and f^f_w that parameterize, respectively, the wheel tread and the wheel flange.
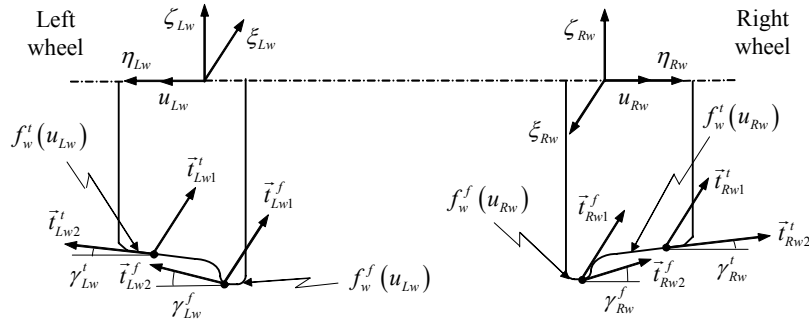
Figure 24 - Tangent vectors to the left and right wheel surfaces

To find the location of the contact points it is necessary the definition of two tangent vectors to the wheel surface, $\mathbf{t}_{w1}$ and $\mathbf{t}_{w2}$, at the point of contact. For the left and right wheels the tangent vectors, represented in Fig. 23, are

$$
\begin{aligned}
\mathbf{t}^l_{Lw1} &= \mathbf{A}_{ws}\,\mathbf{A}_{Lw}\,\mathbf{t}'^l_{Lw1} \qquad ; \qquad l = t, f \\
\mathbf{t}^l_{Rw1} &= \mathbf{A}_{ws}\,\mathbf{A}_{Rw}\,\mathbf{t}'^l_{Rw1} \qquad ; \qquad l = t, f
\end{aligned}
\tag{37}
$$

where vectors $\mathbf{t}'^l_{Lw1} = \{1 \quad 0 \quad 0\}^T$ and $\mathbf{t}'^l_{Rw1} = \{-1 \quad 0 \quad 0\}^T$ for $l = t, f$, being the quantities with superscripts $(.)^t$ and $(.)^f$ referred to the wheel tread and to the wheel flange, respectively. The second tangent vector, shown in Fig. 24, is:

$$
\begin{aligned}
\mathbf{t}^l_{Lw2} &= \mathbf{A}_{ws}\,\mathbf{A}_{Lw}\,\mathbf{t}'^l_{Lw2} \qquad ; \qquad l = t, f \\
\mathbf{t}^l_{Rw2} &= \mathbf{A}_{ws}\,\mathbf{A}_{Rw}\,\mathbf{t}'^l_{Rw2} \qquad ; \qquad l = t, f
\end{aligned}
\tag{38}
$$

where vectors $\mathbf{t}'^l_{Lw2} = \{0 \quad \cos\gamma^l_{Lw} \quad \sin\gamma^l_{Lw}\}^T$ and $\mathbf{t}'^l_{Rw2} = \{0 \quad \cos\gamma^l_{Rw} \quad \sin\gamma^l_{Rw}\}^T$, for for $l = t, f$, and γ^l_{Lw} and γ^l_{Rw} are the contact angles, measured in the cross-sectional plane. These angles are defined between the vectors tangent to the left and right wheel surfaces $\mathbf{t}_{w2}$, at the contact point, and the corresponding local axis η_{Lw} and η_{Rw}, as shown in Fig. 24. The contact angles are obtained by differentiating the functions f^t_w and f^f_w, which define the wheel tread and flange profiles, with respect to the surface parameters u_{Lw} and u_{Rw}, as:

$$
\gamma^l_{Lw} = \mathrm{tg}^{-1}\left(\frac{df^l_w\left(u^l_{Lw}\right)}{du^l_{Lw}}\right) \qquad ; \qquad \gamma^l_{Rw} = \mathrm{tg}^{-1}\left(\frac{df^l_w\left(u^l_{Rw}\right)}{du^l_{Rw}}\right) \qquad ; \qquad l = t, f
\tag{39}
$$

Rail-wheel contact detection

Let the generalized geometry of the rail and wheel be described by generalized surfaces resulting from sweeping the rail profile along the rail centerlines and the wheel profiles around the base circle of the wheel. In order to ensure that the search for the contact points is between convex surfaces, the wheel profile is divided in treat and flange profiles. The contact between the rail and one of the wheel surfaces is described generically in Fig. 25, where the mating surfaces are represented as free surfaces.
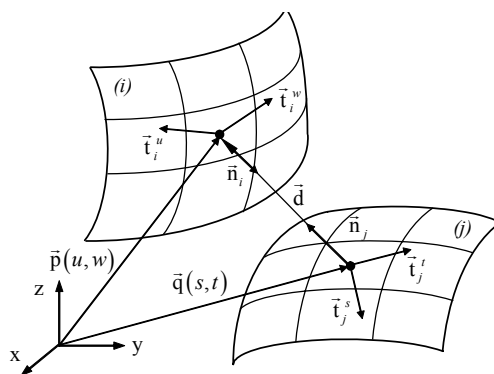
Figure 25 - Candidates to contact points between two parametric surfaces

The geometric conditions for contact between the convex surfaces are defined by vector products defined between the surfaces. The first condition is that the surfaces normals $\mathbf{n}_i$ and $\mathbf{n}_j$ at the candidates to contact points have to be parallel. This condition means that $\mathbf{n}_j$ has null projections over the tangent vectors $\mathbf{t}_i^u$ and $\mathbf{t}_i^w$:

$$\mathbf{n}_j \times \mathbf{n}_i = \mathbf{0} \iff \begin{cases} \mathbf{n}_j^T \mathbf{t}_i^u = 0 \\ \mathbf{n}_j^T \mathbf{t}_i^w = 0 \end{cases} \tag{40}$$

The second condition is that the vector $\mathbf{d}$, which represents the distance between the candidates to contact points, has to be parallel to the normal vector $\mathbf{n}_i$. This condition is mathematically written as:

$$\mathbf{d} \times \mathbf{n}_i = \mathbf{0} \iff \begin{cases} \mathbf{d}^T \mathbf{t}_i^u = 0 \\ \mathbf{d}^T \mathbf{t}_i^w = 0 \end{cases} \tag{41}$$

The geometric conditions (40) and (41) provide four nonlinear equations with four unknowns, the four parameters u, w, s and t that define the two surfaces. This system of equations provides solutions for the location of the candidates to contact points that have to be sorted out. The coordinates of the candidates to contact points are determined by solving an optimal problem and the distance between such points is calculated in the process. The points are in contact if

$$\mathbf{d}^T \mathbf{n}_j \leq 0 \tag{42}$$

When contact is detected, the normal force is calculated using Eq. (10) and the tangential forces are evaluated using the Kalker theory, the Polach formulation or the Heuristic nonlinear creep model.

Tangential contact forces

According to the Kalker linear theory (Kalker, 1979), the longitudinal F_ξ and lateral F_η components of the creep force and the spin creep moment M_ϕ that develop in the wheel-rail contact region are expressed as:

$$\begin{Bmatrix} F_\xi \\ F_\eta \\ M_\phi \end{Bmatrix} = -\,\mathrm{G}\,a\,b \begin{bmatrix} c_{11} & 0 & 0 \\ 0 & c_{22} & \sqrt{ab}\,c_{23} \\ 0 & -\sqrt{ab}\,c_{23} & ab\,c_{33} \end{bmatrix} \begin{Bmatrix} \upsilon_\xi \\ \upsilon_\eta \\ \phi \end{Bmatrix} \tag{43}$$

where G is the combined shear modulus of rigidity of wheel and rail materials and a and b are the semi-axes of the contact ellipse that depend on the material properties and on the normal contact force N, calculated using the normal contact model described by Eq. (10). The parameters c_{ij} are the Kalker creepage and spin coefficients that are tabulated (Kalker, 1990) and only depend on the combined Poisson's ratio v of wheel and rail materials and on the semi-axes ratio a/b of the contact ellipse. The quantities υ_ξ, υ_η and ϕ represent the longitudinal, lateral and spin creepages at the contact point, respectively. The creep forces and the spin creep moment, together with the normal contact forces, define the contact loads resulting from the wheel-rail interaction. These loads are introduced in the equations of motion of the multibody formulation by adding them to the vector of external applied forces of the system model.

For sufficiently small values of creep and spin, the linear theory of Kalker, embodied in Eq. (43), is adequate to determine the creep forces. For larger values, this formulation is no more appropriated since it does not include the saturation effect of the friction forces, i.e., it does not assure that $F_\upsilon \leq \mu N$. In many situations, for example curve negotiation, the inclusion of the saturation effect is crucial due to the existence of slip (Shen, et al., 1983). The Polach

formulation (Polach, 1999) is an alternative creep force model where the longitudinal and lateral components of the creep force that develop in the wheel-rail contact region are expressed as:

$$F_\xi = F \frac{\upsilon_\xi}{\upsilon_C} \qquad ; \qquad F_\eta = F \frac{\upsilon_\eta}{\upsilon_C} + F_{\eta S} \frac{\phi}{\upsilon_C} \qquad (44)$$

where F is the tangential contact force caused by longitudinal and lateral creepages, υ_c is the modified translational creepage, which accounts the effect of spin creepage, and $F_{\eta S}$ is the lateral tangential force caused by spin creepage. The Polach algorithm requires as input the creepages υ_ξ, υ_η and ϕ, the normal contact force N, the semi-axes a and b of the contact ellipse, the combined modulus of rigidity of wheel and rail materials G, the friction coefficient μ and the Kalker creepage and spin coefficients c_{ij}. As a result, the algorithm computes the values for the creep force components F_ξ and F_η. It has been found that for the Polach formulation provides the best approach for the tangent forces, and it is used hereafter (Pombo and Ambrósio, 2004).

Application to the study of a railway vehicle

The wheel-rail contact model outlined here is used to model the ML95 trainset, shown in Fig. 14, which is used by the Lisbon subway company (ML) for passengers' traffic.

Motor   Trailer   Motor
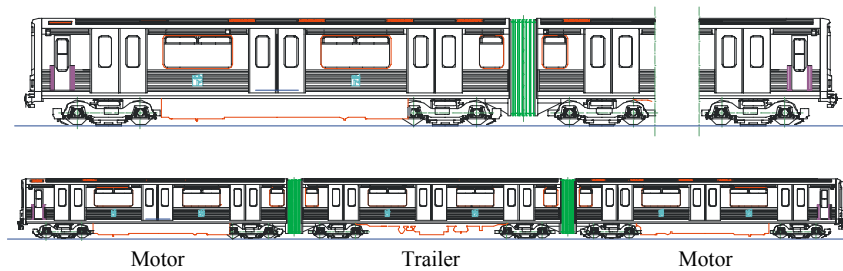
Figure 26 - Schematic representation of the ML95 trainset

The multibody model of the trailer vehicle of the train, developed in the work by Pombo (2004), is composed of the car shell suspended by a set of springs, dampers and other rigid connecting elements on the bogies. This assembly of connective elements constitutes the secondary suspension, sketched in Fig. 26, which is the main responsible for the passenger's comfort.
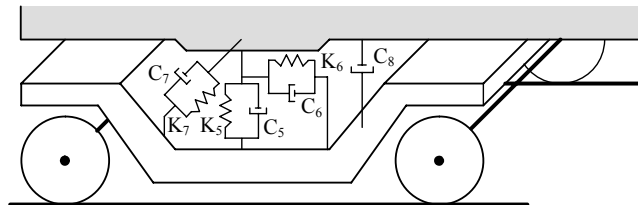

Figure 26 - Secondary suspension model of the ML95 trailer vehicle

The connections between the bogies chassis and the wheelsets, also achieved by another set of springs, dampers and rigid connecting elements, constitute the primary suspension represented in Fig. 27. The primary suspension is the main responsible for the vehicle running stability.
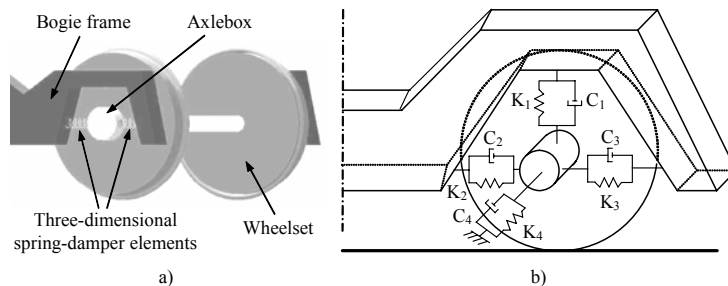

a)   b)

Figure 27 - Primary suspension model of the ML95 trailer bogie: a) Three-dimensional spring-damper elements; b) Suspension model with springs and dampers
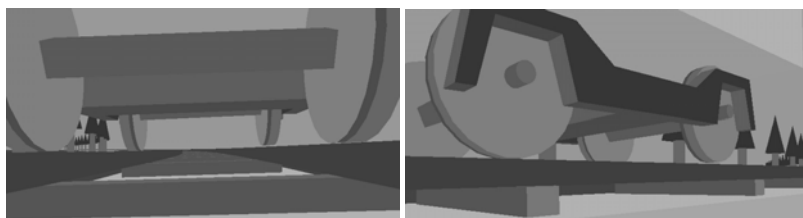
Figure 28 - Lift of the right wheel of the leading wheelset for vehicle forward velocities of 10 and 20 m/s, using the Kalker linear theory

The simulation results of the vehicle, running in a circular track with a radius of 200m with velocities of 10 and 20 m/s, show that the prediction of flange contact is of fundamental importance. Fig. 28 shows that contact forces obtained with the Kalker linear theory originate the lift of the outer wheel of the front wheelset at the entrance of the curve. Despite this wheel lift, derailment does not occur and the analysis proceeds up to end. Nevertheless, such results are not realistic since the existence of flange contact involves high creepages, which makes the Kalker linear theory inappropriate to compute the creep forces. Therefore only the Polach creep force models must be considered.
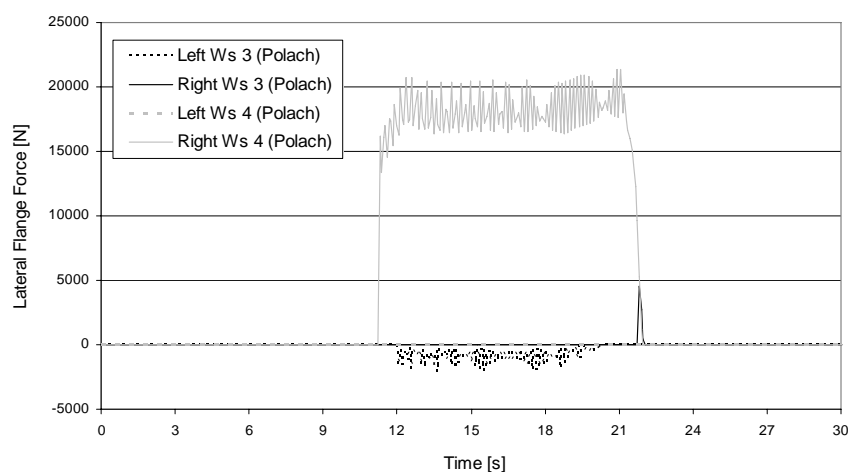
Figure 29 - Lateral flange forces on the wheels of the front bogie for a vehicle forward velocity of 10 m/s

Another aspect to note is that flange contact is detected with all creep force models. Even when running at the speed of 10 m/s, where the centrifugal forces effect is balanced by the track cant, flange contact occurs. Lateral flange forces develop on the wheels of both wheelsets of the front bogie as presented in Fig. 29 for a vehicle forward velocity of 10 m/s and using the Polach creep force model. During curve negotiation, the outer wheel of the leading wheelset and the inner wheel of the rear wheelset have permanent flange contact.

Train crashworthiness

Up to recent years railway vehicles have been designed without any concerns in terms of their structural integrity in the event of a crash. It has been only in the past decade that train passive safety has received attention and that some specifications in terms of their structural ability to absorb energy and to deform in a controlled manner have been defined. The multibody methodologies have the ability not only to represent the major mechanical components of the train but can also to present models for the structural behavior of the train during impact conditions. The development of train models for crashworthiness and their validation with respect to experimental tests is presented here.

The type of test collision scenario, that is used here to validate the design of the energy absorbing components of the train vehicle, is displayed in Fig. 30. The corresponding multibody model includes three cars, for which the individual models are described in detail by Milho, Ambrósio and Pereira (2003).
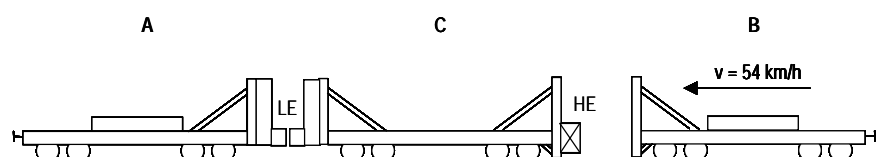

Figure 30 - Collision scenario for the numerical simulation and for an experimental test

The topology of each train car represented in Fig. 31 is used to model the three vehicles involved in the test. Five rigid bodies, B_1 through B_5 represent the passenger compartment, boggie chassis and deformable end extremities. The relative motion between the multibody components is restricted by revolute joints, R_1 and R_2, and by translation joints, T_1 and T_2. The inertia properties of the system components and the location of each component of the train cars are described in references (Milho, Ambrósio and Pereira, 2003 and 2004). For the bogies, the masses of bodies B_2 and B_3 are considered to be 1600 kg. The wheels and axles have a mass of 2800 kg and move only in x direction. The initial positions of the bodies along y are obtained considering that the static position of the global center of mass of group of bodies that define car-bodies A, B and C. The initial positions of the rigid bodies are obtained from the car-bodies geometries.
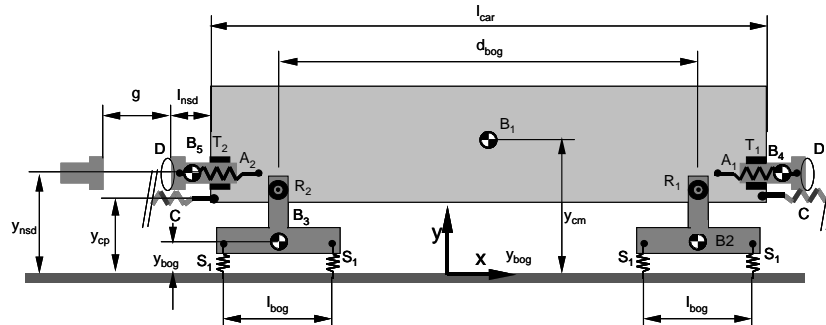
Figure 31 - Car-body model for a single car

Two energy absorption regions of the train car-bodies are identified in terms of their ability to absorb energy during a crash. The high-energy zone corresponds to the structure designed to absorb by plastic deformation significant amounts of energy, located in the train extremities. The low energy zones refer to the regions of the car-bodies where potential impact can occur between consecutive cars of the same trainset, which are generally required to absorb lower levels of energy. During a collision the energy absorption in the train occurs at the low-energy zones, due to the couplers and buffers deformations, and at the high-energy ends, in virtue of the car-end structure deformation. The structural behavior of the coupler, shown as element C in Fig. 31, is represented by a deformation element, with characteristics depicted by Fig. 32(a). The buffers, represented behind element D in Fig. 31, have the force-displacement characteristics, obtained by a detailed finite element analysis presented in Fig. 32(b). The experimental testing a honeycomb structure, with the energy absorbing capabilities similar to the original car-body end structure, is used to represent the high-energy zone, with the initial force-displacement characteristics described in Fig. 32(c).
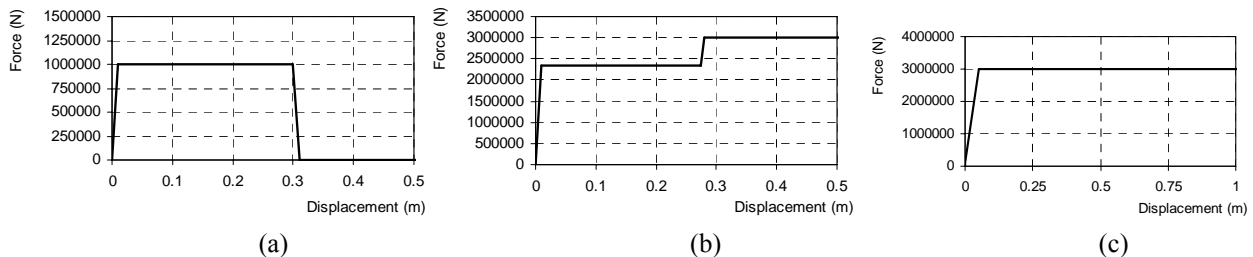

(a)　　　　　　　　　　　(b)　　　　　　　　　　　(c)

Figure 32 - Force-displacement curves of structural elements: (a) Coupler; (b) Buffer; (c) High-energy end

The car-body suspension system involves four suspension spring elements S_1. When the suspension springs are deformed beyond their working range the compression jounce stops and the traction lift-off stops are reached. The contacts between anti-climbers devices in the car-body extremities, represented in Fig. 31 by elements D, use the contact model given by Eq. (10) for the normal forces and a stick model for the tangential forces. In the contact model it is assumed that the equivalent stiffness, for the normal contact between incoming surfaces, is 10^8 N/m. Moreover, it is assumed that the contact is fully plastic, which leads to the null restitution coefficient used in the continuous contact law.
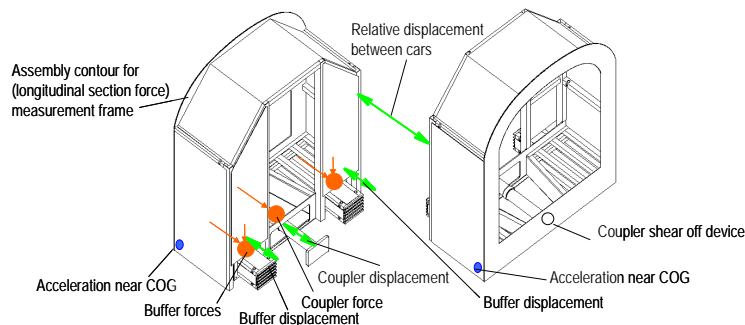

Figure 33 - Location of the measurement instrumentation on the Low-Energy interface
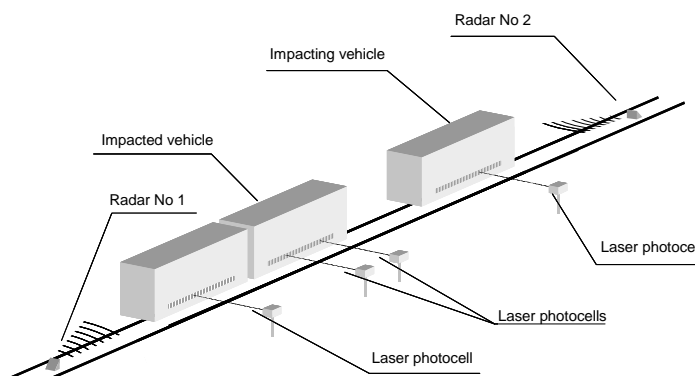
Figure 34 - Photocells used in to measure the vehicles velocity in the experimental test

An experimental test is performed with the purpose of validating the structural low-energy end design of the carbody, developed within the framework of project SAFETRAIN (2001). The experimental test configuration is depicted in Fig. 30. The vehicles are instrumented in order to be possible to measure the accelerations, in given points, the forces transmitted in the buffers and coupler and the relative displacements between system components. This setup is briefly described by Fig. 33. High-speed video cameras are used to monitor the crash and to record the displacement of particular parts of the vehicles, as shown in Fig. 34.

The velocities of the three cars throughout the simulation and experimental test are plotted in Fig. 35. There it is observed that the velocities predicted by the model are very similar to those observed in the experimental test. Furthermore, the levels of energy absoption predicted by the multibody models for the different structural devices of the train are similar to those measured during the experimental test, as summarized in Tab. 1.
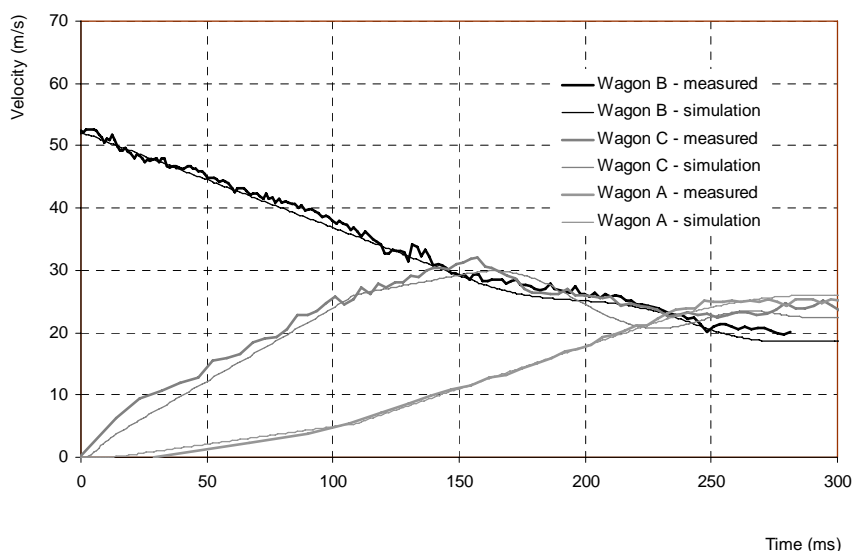

Figure 35 - Time history for the wagons in the simulation and experimental test

The crushing of the high-energy end device was incomplete, also as it was required by the constraint imposed to the optimization problems. For a more detailed description of the simulation and experimental results the interested reader is referred to reference (Milho, Ambrósio and Pereira, 2003).

Table 1 - Energy dissipation distributions in the different components of the train

Component	Simulation	Test	Remarks
Buffers	Wagon C: 624 kJ Wagon A: 373 kJ Total: 997 kJ	280 kJ	The result does not include deformations behind the buffers. No structural deformation occurs in the simulation
Coupler	300 kJ	835 kJ	Test data includes structural deformation behind the coupler
Low energy end	1297 kJ	1435 kJ	Test data includes structural deformation behind the coupler and buffers
Front Honeycomb	2780 kJ	3016 kJ	
Total Energy Absorption	4077 kJ	4451 kJ	

FLEXIBLE MULTIBODY SYSTEMS

Let the principle of the virtual works be used to express the equilibrium of the flexible body in the current configuration $t+\Delta t$ and an updated Lagrangean formulation be used to obtain the equations of motion of the flexible body. Let the finite element method be used to represent the equations of motion of the flexible body. Referring to Fig. 36, the assembly of all finite elements used in the discretization of a single flexible body results in its equations of motion written as (Ambrósio, 1996b)

$$\begin{bmatrix} \mathbf{M}_{rr} & \mathbf{M}_{rf} & \mathbf{M}_{rf} \\ \mathbf{M}_{\phi r} & \mathbf{M}_{\phi\phi} & \mathbf{M}_{\phi f} \\ \mathbf{M}_{fr} & \mathbf{M}_{f\phi} & \mathbf{M}_{ff} \end{bmatrix} \begin{bmatrix} \ddot{\mathbf{r}} \\ \dot{\boldsymbol{\omega}}' \\ \ddot{\mathbf{u}}' \end{bmatrix} = \begin{bmatrix} \mathbf{g}_r \\ \mathbf{g}'_\phi \\ \mathbf{g}'_f \end{bmatrix} - \begin{bmatrix} \mathbf{s}_r \\ \mathbf{s}'_\phi \\ \mathbf{s}'_f \end{bmatrix} - \begin{bmatrix} \mathbf{0} \\ \mathbf{0} \\ \mathbf{f} \end{bmatrix} - \begin{bmatrix} \mathbf{0} & \mathbf{0} & \mathbf{0} \\ \mathbf{0} & \mathbf{0} & \mathbf{0} \\ \mathbf{0} & \mathbf{0} & \mathbf{K}_L + \mathbf{K}_{NL} \end{bmatrix} \begin{bmatrix} \mathbf{0} \\ \mathbf{0} \\ \mathbf{u}' \end{bmatrix} \tag{46}$$

where $\ddot{\mathbf{r}}$ and $\dot{\boldsymbol{\omega}}'$ are respectively the translational and angular accelerations of the body fixed reference frame and $\ddot{\mathbf{u}}'$ denotes the nodal accelerations measured in body fixed coordinates. The local coordinate frame $\xi\eta\zeta$, attached to the flexible body, is used to represent the gross motion of the body and its deformation.
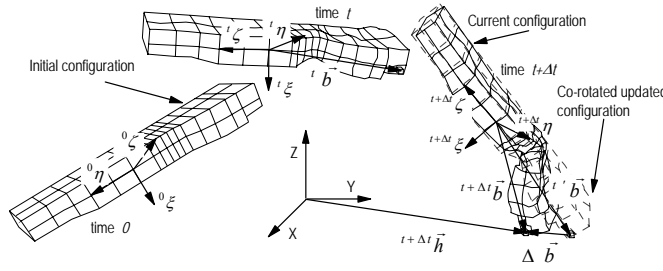

Figure 36 - General motion of a flexible body

Linear Deformations of Flexible Bodies

In many situations it is enough to consider that the components of the multibody system only experience linear elastic deformations. Furthermore, assume that the mode superposition technique can be used. Then, the flexible part of the body is described by a sum of selected modes of vibration as

$$\mathbf{u}' = \mathbf{X}\,\mathbf{w} \tag{47}$$

where the vector $\mathbf{w}$ represents the contributions of the vibration modes towards the nodal displacements and $\mathbf{X}$ is the modal matrix. Due to the reference conditions, the modes of vibration used here are constrained modes. Due to the assumption of linear elastic deformations the modal matrix is invariant. The reduced equations of motion for a linear flexible body are (Augusta Neto and Ambrósio, 2004)

$$\begin{bmatrix} \mathbf{M}_r & \mathbf{M}_{rf}\mathbf{X} \\ \mathbf{X}^T\mathbf{M}_{fr} & \mathbf{I} \end{bmatrix} \begin{Bmatrix} \ddot{\mathbf{q}}_r \\ \ddot{\mathbf{w}} \end{Bmatrix} = \begin{Bmatrix} \mathbf{g}_r \\ \mathbf{X}^T\mathbf{g}_f \end{Bmatrix} - \begin{Bmatrix} \mathbf{s}_r \\ \mathbf{X}^T\mathbf{s}_f \end{Bmatrix} - \begin{Bmatrix} \mathbf{0} \\ \boldsymbol{\Lambda}\mathbf{w} \end{Bmatrix} \tag{48}$$

where $\boldsymbol{\Lambda}$ is a diagonal matrix with the squares of the natural frequencies associated to the modes of vibration selected. For a detailed discussion on the selection of the modes used the interested reader is referred to (Yoo and Haug, 1986).

Nonlinear Deformations

For flexible multibody systems experiencing nonlinear geometric and material deformations the motion for a flexible body is described by Eq. (48). However, due to the time variance of all its coefficients, Eq. (48) is not efficient for computational implementation. Instead, by considering a lumped mass formulation for the mass matrix and referring the nodal accelerations to the inertial frame, the equations of motion for a single flexible body become (Ambrósio, 1996b)

$$\begin{bmatrix} m\mathbf{I} + \bar{\mathbf{A}}\underline{\mathbf{M}}^*\bar{\mathbf{A}}^T & -\bar{\mathbf{A}}\underline{\mathbf{M}}^*\mathbf{S} & \mathbf{0} \\ -\left(\bar{\mathbf{A}}\underline{\mathbf{M}}^*\mathbf{S}\right)^T & \mathbf{J}' + \mathbf{S}^T\underline{\mathbf{M}}^*\mathbf{S} & \mathbf{0} \\ \mathbf{0} & \mathbf{0} & \mathbf{M}_{ff} \end{bmatrix} \begin{bmatrix} \ddot{\mathbf{r}} \\ \dot{\boldsymbol{\omega}}' \\ \ddot{\mathbf{q}}'_f \end{bmatrix} = \begin{bmatrix} \mathbf{f}_r + \bar{\mathbf{A}}\mathbf{C}'_\delta \\ \mathbf{n}' - \tilde{\boldsymbol{\omega}}'\mathbf{J}'\boldsymbol{\omega}' - \mathbf{S}^T\mathbf{C}'_\delta - \bar{\mathbf{I}}^T\mathbf{C}'_\theta \\ \mathbf{g}'_f - \mathbf{f} - \left(\mathbf{K}_L + \mathbf{K}_{NL}\right)\mathbf{u}' \end{bmatrix} \tag{49}$$

where the absolute nodal displacements are written as

$$\ddot{\mathbf{q}}'_{kf} \equiv \begin{bmatrix} \ddot{\mathbf{d}}' \\ \ddot{\boldsymbol{\alpha}}' \end{bmatrix}_k = \ddot{\mathbf{u}}'_k + \begin{bmatrix} \mathbf{A}^T & -\left(\tilde{\mathbf{x}}_k + \tilde{\boldsymbol{\delta}}_k\right)' \\ \mathbf{0} & \mathbf{I} \end{bmatrix} \begin{bmatrix} \ddot{\mathbf{r}} \\ \dot{\boldsymbol{\omega}}' \end{bmatrix} + \begin{bmatrix} \tilde{\boldsymbol{\omega}}'\tilde{\boldsymbol{\omega}}'\left(\mathbf{x}_k + \boldsymbol{\delta}_k\right)' + 2\tilde{\boldsymbol{\omega}}'\dot{\boldsymbol{\delta}}'_k \\ \tilde{\boldsymbol{\omega}}'\dot{\boldsymbol{\theta}}'_k \end{bmatrix} \tag{50}$$

being $\mathbf{x}_k$ the position of node k in the reference configuration. In Eq. (49) $\underline{\mathbf{M}}^*$ is a diagonal mass matrix containing the mass of the $\underline{n}$ boundary nodes, $\overline{\mathbf{A}}^T = [\mathbf{A} \quad \cdots \quad \mathbf{A}]^T$, $\mathbf{S} = [(\tilde{\mathbf{x}}'_1 + \tilde{\boldsymbol{\delta}}'_1)^T \quad \cdots \quad (\tilde{\mathbf{x}}'_{\underline{n}} + \tilde{\boldsymbol{\delta}}'_{\underline{n}})^T]^T$ and $\overline{\mathbf{I}} = [\mathbf{I} \quad \cdots \quad \mathbf{I}]^T$ where $\mathbf{A}$ is the transformation matrix from the body fixed to global coordinate coordinates and $\mathbf{x}_k$ denotes the position of node k. Vectors $\mathbf{C}'_\delta$ and $\mathbf{C}'_\theta$ represent respectively the reaction force and moment of the flexible part of the body over the rigid part, given by

$$\begin{aligned} \mathbf{C}'_\delta &= \mathbf{g}'_\delta - \mathbf{F}_\delta - \left(\mathbf{K}_L + \mathbf{K}_{NL}\right)_{\delta\delta} \boldsymbol{\delta}' - \left(\mathbf{K}_L + \mathbf{K}_{NL}\right)_{\delta\theta} \boldsymbol{\theta}' \\ \mathbf{C}'_\delta &= \mathbf{g}'_\theta - \mathbf{F}_\theta - \left(\mathbf{K}_L + \mathbf{K}_{NL}\right)_{\theta\delta} \boldsymbol{\delta}' - \left(\mathbf{K}_L + \mathbf{K}_{NL}\right)_{\theta\theta} \boldsymbol{\theta}' \end{aligned} \tag{51}$$

The coupling between the rigid body motion and the system deformations is fully preserved. For a more detailed description of the formulation, and the notation, the interested reader is referred to reference (Ambrósio, 1996b).

Applications to the design of space structures

The methodology describing the linear flexibility of multibody systems is demonstrated through the application to the simulation of the unfolding of a satellite antenna, the Synthetic Aperture Radar (SAR) antenna, which is a part of the European research satellite ERS-1, represented in Fig. 37. During the transportation the antenna is folded, in order to occupy as little space as possible and afterwards unfolds to take the functional configuration (Anantharaman, 1987).
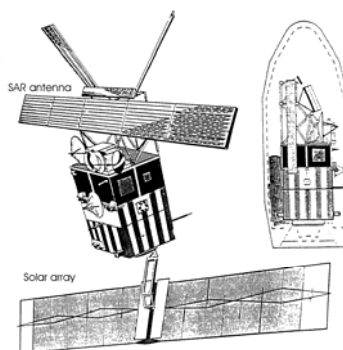

Figure 37 - The European satellite with the folded and unfolded configurations of the antenna

The SAR antenna consists in two identical subsystems, each with three coupled four-bar links that unfold two panels on each side. The central panel is attached to the main body of the satellite. Each unfolding system has two degree of freedom, driven individually by actuators located in joints A and B, shown in Fig. 38. All bodies of the model are made of a carbonfiber reinforced plastic with a specific mass of 1610 Kg/m3. Each panel is 1.994 m long by 1.3 m wide and has a thickness of 2 mm.

In the first phase of the unfolding process the panel 3 is rolled out, around an axis normal to the main body, by a rotational spring-damper-actuator in joint A, while the panel 2 is held down by blocking joints D and E. The second phase begins with the joint A blocked, next the panels 2 and 3 are swung out to the final position by a rotational spring-damped-actuator.
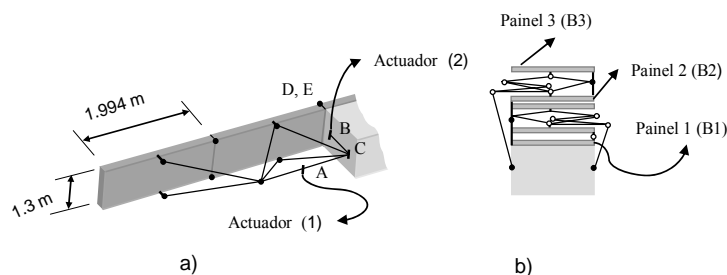

Figure 38 - The SAR antenna: a) one half unfolded state b) folded antenna.

The model used for one half of the folding antenna, schematically depicted Fig. 39, is composed by 12 bodies, 16 spherical joints and 3 revolute joints. The central panel is attached to the satellite, defined as body 1, which has much higher mass and inertias. The data for this antenna is reported in the work of Anantharamann (1987).
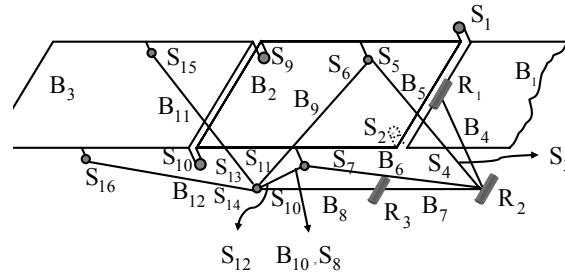
Figure 39 - Multibody model of the SAR antenna.

A rotational actuator moment responsible for the start of the unfolding must be correctly designed so that the mechanism starts without jamming and without shocks. Because the satellite is a very light and flexible structure the use of a rigid multibody model for the system can suggest a design that leads to failure of the unfolding process. The angular velocity of panel 3, predicted by the rigid and flexible multibody models of the antenna are shown in Fig. 40. There, it is clearly visible that large vibrations are excited during the unfolding process, which cannot be neglected when comparing the rigid with the flexible models results.
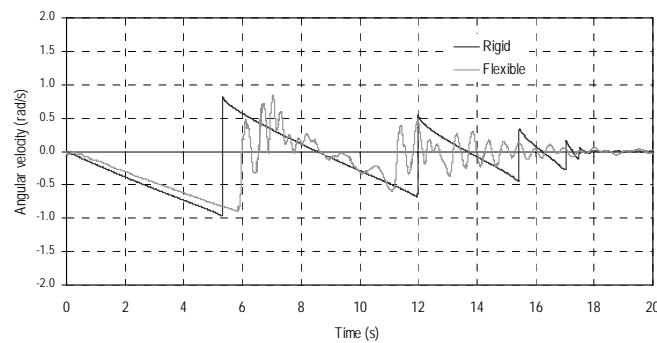
Figure 40 - Angular velocity of panel 3 for the rigid and flexible antenna.

The complete unfolding process of the antenna is described in Fig.41 by a sequence of images obtained for the simulation of the unfolding process with the flexible multibody model.
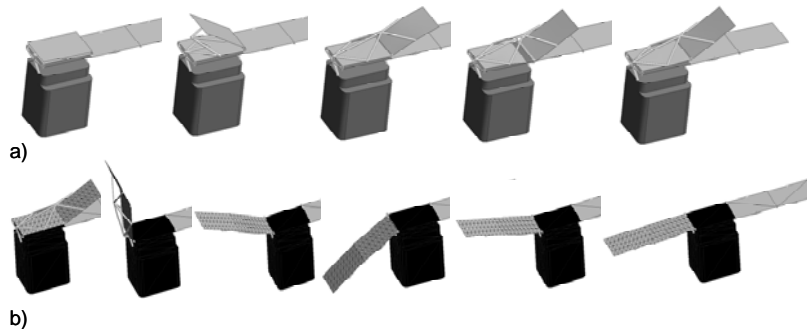

Figure 41 - Configuration of the antenna unfolded process: a) in the first phase b) in the second phase.

The fully spatial model of the satellite antenna, made of composite materials, allows for capturing deformation effects that are not represented by other models. The orientation of the different layers of the composites influence, in particular, the torsion modes of vibration of the panels, which play a very important role in the deployment, as observed in Fig. 42 with the displacements of two points that would have been equal if the unfolding process had been planar as predicted by the rigid multibody model. This torsion deformation, which is sensitive to the layer orientations, leads to important differences in the actuator angles history. This discrepancy can result from the difference between the vibration modes of the both models.

The use of flexible multibody dynamics in the framework of composite structural modeling opens new possibilities for complex systems design. Such complex models are also used in the framework of the optimization of complex systems or in the design of smart structures. A complete description of this work in the framework of optimization of flexible multibody systems can be found on reference (Augusta Neto, 2006).
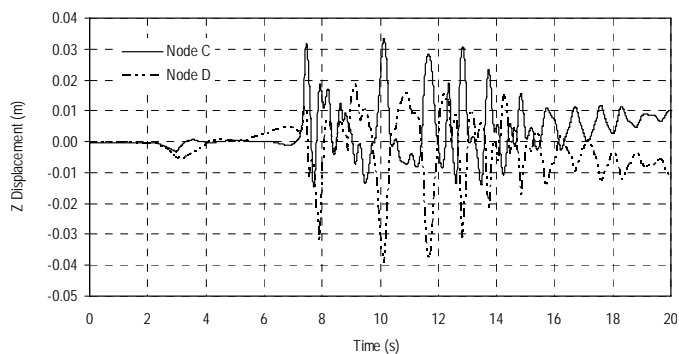
Figure 42 - Normal displacement of nodes C and D, coinciding with S_9 and S_{10} on the flexible panel 2, in the unfolding process.

Vehicle dynamics applications

The formulations reported here are applied to the dynamic multibody model of a sports car, the Lancia Stratos presented in Fig. 43. The vehicle, a replica of the original Lancia, was assembled in-house at IDMEC/IST, providing an opportunity to obtain through direct measurements the structural and dynamic characteristics of all car components used. Two multibody models of the vehicle, composed of 17 bodies, are considered here. The system components include the front double A-arm suspension system, the rear McPherson suspension system, wheels and chassis as depicted by Fig. 43. The first model has a rigid chassis while the second model has a flexible chassis.

Figure 43 - Prototype of a sports car and its multibody model.

The mass and inertia characteristics and initial positions of the vehicle components are reported by Ambrósio and Gonçalves (2001). To model the tire interaction with the ground an analytical tire model with comprehensive slip is used (Gim and Nikravesh, 1990). In the flexible model of the chassis, the finite element method is used to describe the vehicle deformations. The structural components of the chassis are modeled using 262 beam elements, 121 plate elements and 18 concentrated mass elements, all available in the finite element program ANSYS. The model has 282 nodes, corresponding to a total of 1680 nodal degrees of freedom. The shell of the chassis is not considered in the model due to its small influence in the vehicle structural dynamics. It is assumed that the body fixed referential is attached to a node located in the center of mass of the model.

The natural frequencies and corresponding modes of vibration of the chassis are evaluated considering the reference conditions consistent with the body fixed referential location, i.e., the nodal point located in the center of mass on the finite element mesh is fixed. The first bending mode of vibration is shown in Fig. 44.
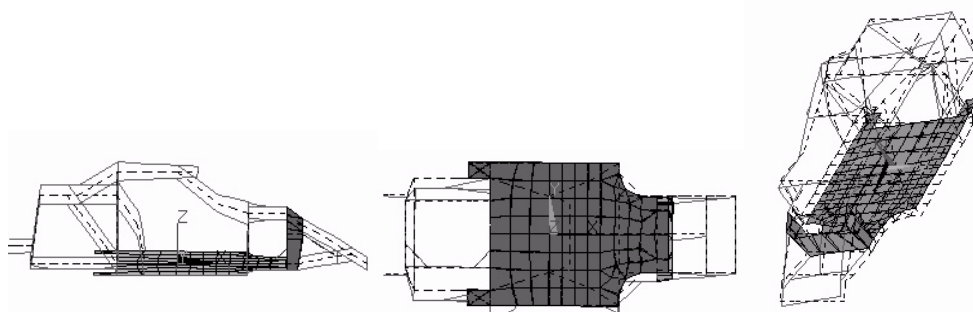

Figure 44 - Bending about XX (ω_4=13.81 Hz).

The directional response ability of a road vehicle is tested with some emergency maneuvers. The case of the obstacle avoidance maneuver, where the vehicle is subjected to very quick steering inputs as shown in Fig. 45, portrays one of the typical tests. The maneuver is simulated here for both rigid and flexible models in three different situations where the vehicle moves at speeds of 60, 90 and 120 km/h. The steering input is the same in all simulations. The results

of the simulation for the flexible model are displayed in Fig. 46 for a velocity of 60 and 120 Km/h. From the results shown in Fig. 47 it can be seen that the flexible model directional response is slightly slower than that of the rigid model that quickly develops the maximum lateral acceleration for the turning situation.
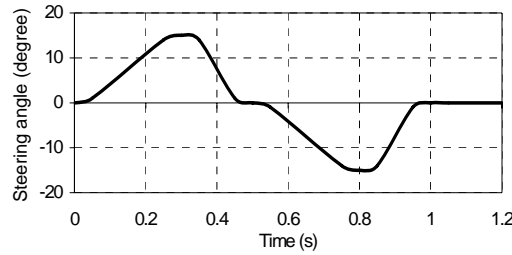

Figure 45 - Steering angle input for the obstacle avoidance.

Both models present a major oversteering for high speeds. The differences observed between the dynamic response of the rigid and flexible model are small due to the high stiffness of the flexible vehicle model.
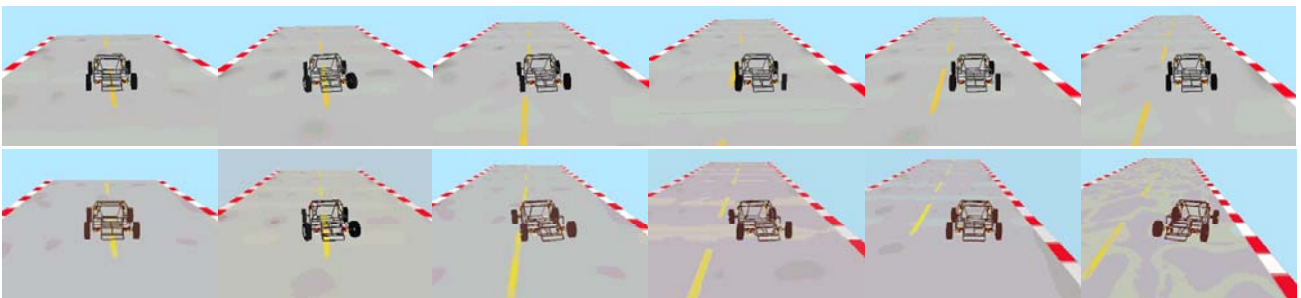

Figure 46 - Simulation of an obstacle avoidance maneuver for 60 km/h(top) and 120 km/h(bottom).
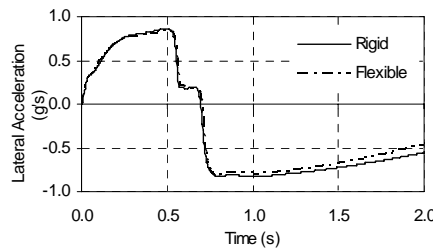

Figure 47 - Lateral acceleration of the vehicle CM for the rigid and the flexible model, at 120 km/h.

The flexible chassis model allows the evaluation of the local deformation of the chassis during the different simulations. In Fig. 48 the nodal displacements of the node where the upper arm of the front left suspension is attached are plotted. The results show that the lateral displacements increase with the vehicle velocity. This type of data can be used, in a post processing phase, to study the vehicle durability and evaluate maximum deformations and their relations to speeds and lateral accelerations that would not have been possible to obtain with the rigid model.
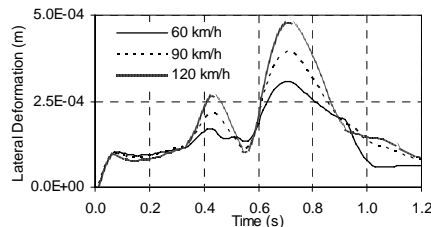

Figure 32 Lateral displacement in the front suspension joint between upper arm and chassis.

CONCLUSIONS

The multibody dynamics formalisms provide an extremely efficient framework to incorporate different disciplines. The behavior of a good number of phenomena in different problems can be represented by kinematic constraints (e.g., contact, muscle action, guidance) or by contact forces (e.g, impact phenomena, control, general interactions). However, different disciplines use different preferred numerical methods to solve their equilibrium equations which lead to difficulties in the co-simulation of different systems. The use of multibody formalisms in vehicle dynamics presents a strong increase due to the suitability to model contacts, general joints, data processing, etc. The treatment of structural components with large rotations or of rotating bodies with structural deformations finds in the flexible multibody dynamics efficient methods to deal with the problem. A continued effort to close the gap between the flexible multibody dynamics and the nonlinear finite element method is required. The need for more robust and efficient numerical methods to handle the specific forms of the MBS equations and the discontinuities associated to intermittent and 'fast' behaviors are still required.

ACKNOWLEDGMENTS

REFERENCES

Ambrósio, J. and Nikravesh, P., 1992, "Elastic-Plastic Deformation in Multibody Dynamics", Nonlinear Dynamics, Vol. 3, pp. 85-104.

Ambrósio, J., Pereira, M. and Dias, J., 1996a, "Distributed and Discrete Nonlinear Deformations on Multibody Systems", Nonlinear Dynamics, Vol.10, No.4, pp. 359-379.

Ambrósio, J., 1996b, "Dynamics of Structures Undergoing Gross Motion and Nonlinear Deformations: A Multibody Approach", Computers and Structures, Vol.59, No.6, pp. 1001-1012.

Ambrósio, J. and Gonçalves, J., 2001, "Vehicle Crashworthiness Design and Analysis by Means of Nonlinear Flexible Multibody Dynamics", Int. J.of Vehicle Design, Vol.26, No.4, pp. 309-330.

Ambrósio, J. and Silva, M., 2005, "A Biomechanical Multibody Model with a Detailed Locomotion Muscle Apparatus", in Advances in Computational Multibody Systems (J. Ambrósio, Ed.), Springer, Dordrecht, The Netherlands, pp. 155-184.

Anantharaman, M., 1987, "The Dynamic Analysis of Flexible Mechanisms Using Finite Element Methods", D.-Ing. Thesis, University of Stuttgart, Sttutgart, Germany.

Antos, P., and Ambrósio, J., 2004, "A Control Strategy Of A Vehicle Multibody Model For Trajectory Tracking", Multibody Systems Dynamics, Vol.11, No.4, pp. 365-394.

Brüls, O., Duysinx, P. and Golinval, J.-C., 2006, "A Model Reduction Method for the Control of Rigid Mechanisms", Multibody Systems Dynamics, DOI: 10.1007/s11044-006-1354-8.

Cardona, A. and Geradin, M., 1988, "A Beam Finite Element Non Linear Theory with Finite Rotations", Int. J. Nume Methods in Engng., Vol.26, pp. 2403-2438.

Garcia de Jalon, J., Bayo, E., 1994, "Kinematic and Dynamic Simulation of Mechanical Systems – The Real-Time Challenge", Springer-Verlag, Berlin, Germany.

Gear, C.W., 1981, "Numerical Solution of Differential-Algebraic Equations", IEEE Transactions on Circuit Theory, Vol. CT-18, pp. 89-95.

Géradin, M. and Cardona, A., 2001, "Flexible Multibody Dynamics: A Finite Element Approach", John Wiley & Sons, Chichester, United Kingdom.

Gonçalves, J. and Ambrósio, J., 2001, "Complex Flexible Multibody Systems with Application to Vehicle Dynamics", Multibody System Dynamics, Vol. 6, No. 2, pp. 163-182.

Hughes, T., 1987, "The Finite Element Method: Linear Static and Dynamic Finite Element Analysis", Dover Publications Inc, Mineola, New York.

Huston, R. and Wang, Y., 1994, "Flexibility effects in multibody systems", Computer Aided Analysis of Rigid and Flexible Mechanical Systems (M.S. Pereira and J.A.C. Ambrósio, Ed.), Kluwer, Dordrecht, The Netherlands, pp. 351-376.

Huyge, K., Ambrósio, J. and Pereira, M., 2005, "A Control Strategy for the Dynamics of a Motorcycle, Including Rider", Proceedings of EUROMECH Nonlinear Dynamics Conference (ENOC 2005), Eindhoven, The Netherlands, August 7-12.

Irvine, L., Marin, S. and Smith, P., 1986, "Constrained Interpolation and Smoothing", Constructive Approximation, Vol. 2, pp. 129-151.

Johnson, K.L., 1994, "Contact Mechanics", Cambridge University Press, Cambridge, England

Kalker, J. J., 1979, "Survey of Wheel-Rail Rolling Contact Theory", Vehicle System Dynamics, Vol. 8, No. 4, pp. 317-358.

Kalker, J. J., 1990, "Three-Dimensional Elastic Bodies in Rolling Contact", Kluwer Academic Publishers, Dordrecht, The Netherlands.

Kane, T. and Levinson, D., 1985, "Dynamics: Theory and Applications", McGraw-Hill, New York, New York.

Lankarani, H. and Nikravesh P., 1994, "Continuous Contact Force Models For Impact Analysis In Multibody Systems", Nonlinear Dynamics, Vol.5, pp. 193-207.

Lankarani, H., Ma, D. and Menon, R., 1995, "Impact dynamics of multibody mechanical systems and application to crash responses of aircraft occupant/structure", Computational Dynamics in Multibody Systems (M. Seabra Pereira, J. Ambrósio, Eds.), Kluwer, Dordrecht, The Netherlands, pp. 239-265.

Mikkola, A. and Shabana, A., 2003, "A Non-Incremental Finite Element Procedure for the Analysis of Large Deformation of Plates and Shells in Mechanical System Applications", Multibody Systems Dynamics, Vol.9, pp. 283–309.

Milho, J., Ambrósio, J. and Pereira, M., 2003, "Validated Multibody Model for Train Crash Analysis", International Journal of Crashworthiness, Vol. 8, No. 4, pp. 339-352.

Milho, J., Ambrósio, J. and Pereira, J., 2004, "Design of Train Crash Experimental Tests by Optimization Procedures", International Journal of Crashworthiness, Vol. 9, No. 5, pp. 483-493.

Neto M., Ambrósio, J. and Leal, R., 2004, "Flexible Multibody Systems Models Using Composite Materials Components", Multibody Systems Dynamics, Vol. 12, No. 4, pp. 363-405.

Neto M., Ambrósio, J. and Leal, R.,2006, "Composite Materials in Flexible Computational Multibody Dynamics", Computer Methods in Applied Mechanics and Engineering, Vol. 195, pp. 6860-6873.

Nikravesh, P., Chung, I. and Benedict, R., 1983, "Plastic Hinge Approach to Vehicle Crash Simulation", Computers and Structures, Vol.16, No.1-4, pp. 395-400.

Nikravesh P., 1988, "Computer-Aided Analysis of Mechanical Systems", Prentice-Hall, Englewood Cliffs, New Jersey.

Nikravesh, P. and Gim, G., 1993, "Systematic Construction of the Equations of Motion for Multibody Systems Containing Closed Kinematic Loops", Journal of Mechanical Design, Vol. 115, No. 1, pp. 143-149.

Petzold, L., 1994, "Computational challenges in mechanical systems simulation", In Computer-Aided Analysis of Rigid and Flexible Mechanical Systems, (M. Pereira and J. Ambrósio Eds.), Kluwer Academic Publishers, Dordrecht, The Netherlands, pp 483-499.

Pfeiffer, F. and Glocker, C., 1996, "Multibody Dynamics with Unilateral Constraints", John Wiley & Sons, New York, New York.

Polach, O., 1999, "A Fast Wheel-Rail Forces Calculation Computer Code", Vehicle System Dynamics, Supplement 33, pp. 728-739.

Pombo, J. and Ambrósio, J., 2003, "General Spatial Curve Joint for Rail Guided Vehicles: Kinematics and Dynamics", Multibody Systems Dynamics, Vol. 9, pp. 234-264.

Pombo, J. and Ambrósio, J., 2004, "A Multibody Methodology for Railway Dynamics Applications", Technical Report IDMEC/CPM-04/002, IDMEC, Instituto Superior Técnico, Lisboa, Portugal.

Pombo, J. and Ambrósio, J., 2007, "Modelling Tracks for Roller Coaster Dynamics", International Journal of Vehicle Design, (to appear).

Rauter, F., Pombo, J., Ambrósio, J., Chalansonnet, J., Bobillot, A. and Pereira, M., 2007, "Contact Model for the Pantograph-Catenary Interaction", JSME International Journal of System Design and Dynamics, (to appear).

SAFETRAIN, 2001, "Dynamic Tests", SAFETRAIN Technical Report T8.2-F, Deutsche Bann, Berlin, Germany.

Shabana, A., 1989, "Dynamics of Multibody Systems", John Wiley & Sons, New York, New York.

Shampine, L. and Gordon, M., 1975, "Computer Solution of Ordinary Differential Equations: The Initial Value Problem, Freeman", San Francisco, California.

Shen, Z., Hedrick, J. and Elkins, J., 1983, "A Comparison of Alternative Creep Force Models for Rail Vehicle Dynamic Analysis", 8th IAVSD Symposium on Dynamics of Vehicles on Road and Tracks, (J. K. Hedrick, Ed.), Swets and Zeitlinger, Cambridge, Massachussetts, pp. 591-605.

Song, J., and Haug, E., 1980, "Dynamic Analysis of Planar Flexible Mechanisms", Computer Methods in Applied Mechanics and Engineering, Vol.24, pp. 359-381.

Yoo, W.-S. and Haug, E., 1986, "Dynamics of Flexible Mechanical Systems Using Vibration and Static Correction Modes", ASME J. of Mechanisms, Transmissions and Automation in Design, Vol.108, pp. 315-322.